

REPORT DOCUMENTATION PAGE

Form Approved OMB No. 0704-0188

Public reporting burden for this collection of information is estimated to average 1 hour per response, including the time for reviewing instructions, searching existing data sources, gathering and maintaining the data needed, and completing and reviewing the collection of information. Send comments regarding this burden estimate or any other aspect of this collection of information, including suggestions for reducing the burden, to Department of Defense, Washington Headquarters Services, Directorate for Information Operations and Reports (0704-0188), 1215 Jefferson Davis Highway, Suite 1204, Arlington, VA 22202-4302. Respondents should be aware that notwithstanding any other provision of law, no person shall be subject to any penalty for failing to comply with a collection of information if it does not display a currently valid OMB control number.
PLEASE DO NOT RETURN YOUR FORM TO THE ABOVE ADDRESS.

1. REPORT DATE (DD-MM-YYYY) 27-01-2004	2. REPORT TYPE Final Report	3. DATES COVERED (From - To) 14 September 2002 - 14-Sep-03
--	---------------------------------------	--

4. TITLE AND SUBTITLE Dispersion Effects in Nonlinear Light Propagation in 1-D Fiber Gratings	5a. CONTRACT NUMBER FA8655-02-M4087
	5b. GRANT NUMBER
	5c. PROGRAM ELEMENT NUMBER

6. AUTHOR(S) Dr. Carlos Martel	5d. PROJECT NUMBER
	5d. TASK NUMBER
	5e. WORK UNIT NUMBER

7. PERFORMING ORGANIZATION NAME(S) AND ADDRESS(ES) Universidad Politecnica of Madrid Avenida Ramiro de Maeztu,7 Ciudad Universitaria Madrid 28040 Spain	8. PERFORMING ORGANIZATION REPORT NUMBER N/A
---	--

9. SPONSORING/MONITORING AGENCY NAME(S) AND ADDRESS(ES) EOARD PSC 802 BOX 14 FPO 09499-0014	10. SPONSOR/MONITOR'S ACRONYM(S)
	11. SPONSOR/MONITOR'S REPORT NUMBER(S) SPC 02-4087

12. DISTRIBUTION/AVAILABILITY STATEMENT
Approved for public release; distribution is unlimited.

13. SUPPLEMENTARY NOTES

14. ABSTRACT

This report results from a contract tasking Universidad Politecnica of Madrid as follows: The contractor will investigate the use of the so-called nonlinear coupled mode equations (NLCME) to obtain approximate solutions of Maxwell's equations for light propagation in periodic optical fiber structures. In particular, one class of solutions called "Gap Solitons," exhibit the ability to propagate at any speed from zero to the local speed of light, and offer great promise for various optical storage and buffer devices. This project will test the accuracy of the NLCME approximation for the propagation of gap solitons in optical fibers with material dispersion, by comparing NLCME solutions with exact solutions of the Maxwell's equations.

15. SUBJECT TERMS
EOARD, Electromagnetics, Optical Theory, optics

16. SECURITY CLASSIFICATION OF:			17. LIMITATION OF ABSTRACT UL	18. NUMBER OF PAGES 80	19a. NAME OF RESPONSIBLE PERSON DONALD J SMITH
a. REPORT UNCLAS	b. ABSTRACT UNCLAS	c. THIS PAGE UNCLAS			19b. TELEPHONE NUMBER (Include area code) +44 (0)20 7514 4953

Dispersion effects in nonlinear light propagation in 1-D fiber gratings

12th September 2003

Final report to the European Office of Aerospace Research and Development
SPC 02-4087 Contract order number: FA8655-02-M4087

Carlos Martel (martel@fmetsia.upm.es)

José M. Vega

Carlos M. Casas

Depto. Fundamentos Matemáticos

E.T.S.I. Aeronáuticos

Universidad Politécnica de Madrid

28040 Madrid, SPAIN

Contents

1 Introduction	1
2 Maxwell-Lorentz equations	3
3 Envelope equation description	7
4 Continuous wave solutions	15
5 Stability of the CW	19
5.1 Perturbations with $k \sim 1$ wavenumber	20
5.2 Perturbations with small dispersive scales	24
5.3 Numerical simulations of the amplitude equations	29
6 Gap Solitons	38
7 Stability of the Gap Solitons	40
7.1 Perturbations without dispersive scales	41
7.2 Perturbations with dispersive scales	48
7.3 Numerical simulations of the amplitude equations	51
8 Numerical simulations of the MLE	58
9 Concluding remarks	69
Appendix A. Numerical integration of the amplitude equations (33)-(35)	71
Appendix B. Numerical integration of the MLE (16)-(17)	74
References	76

1 Introduction

There is a great deal of current interest in the study of nonlinear propagation of light in periodic structures (see e.g., the recent reviews [1, 2, 3] and the references therein). The combination of the Kerr nonlinearity of the fiber and the periodic variation of the refractive index along the length of the fiber (fiber grating) produces a rich variety of phenomena (bistability, multistability, switching behavior, etc.) that, together with the recent developments in grating fabrication techniques, gives to these periodic structures a very promising potential for use as components in all-optical communication systems.

The localized structures that emerge from the balance between the nonlinearity and the medium periodicity, called gap solitons, exhibit very small formation lengths, enabling nonlinear pulse compression and soliton dynamics to be observed on length scales on the order of centimeters. But possibly the most striking feature of gap solitons is the ability to propagate (in theory) at any speed between zero and the speed of light in the fiber without the grating. This possibility of trapping light (gap soliton propagation at zero speed) is currently a topic of great interest because of its future applications in the production of all optical buffers and storing devices.

The theoretical research on light propagation in fiber gratings is based on the analysis and numerical simulations of the so-called nonlinear coupled mode equations (NLCME). This system of equations accounts for the effect of propagation, nonlinearity and the medium periodicity, and can be derived from the Maxwell-Lorentz equations (MLE) for electromagnetic wave propagation in a dielectric medium assuming that the solution is a superposition of two counterpropagating (backward and forward) fields whose envelopes are slowly modulated on space and time. In the derivation of the NLCME, the material dispersion terms are neglected because (due to the slow envelope description) they are small as compared with the transport terms. But this is a singular problem and the dispersion terms can give rise to small dispersive scales that develop in the propagation time scale. This phenomenon is not captured in the NLCME formulation and its correct description requires to consider small material dispersion terms.

The main purpose of this research project is to validate the widely used NLCME. That is, to determine whether the solutions of the NLCME constitute good approx-

imations of the solutions of the original system (i.e., the material dispersion terms can be safely ignored) or whether the dispersion terms are essential and the NLCME should not be used. As a secondary goal, this research project also aims to describe (applying numerical simulation techniques to the NLCME with dispersion and to the MLE) the solutions that appear when the NLCME are no longer applicable because the system develops small dispersive scales.

This report is organized as follows. In the next Section we introduce our physical model for light propagation on a fiber grating: the one dimensional MLE, and study its basic linear light propagation characteristics. The derivation of the NLCME with material dispersion terms from the MLE is carried out in Section 3. The simplest uniform solutions of the NLCME, namely, the continuous wave solutions, are introduced in Section 4 and its linear stability properties, including the effect of the material dispersion, are analyzed in Section 5, where some numerical simulations of the NLCME with small dispersion are also performed to validate the theoretical predictions. In Section 6 we describe a family of solitary wave pulse-like solutions of the NLCME known as Gap Solitons, and in Section 7 we study its stability properties theoretically (defining and computing the Evans function) and numerically (performing some numerical simulations of the NLCME). Numerical simulations of the MLE are used in Section 8 to carry out a definitive check of the stability results and of the validity of the envelope equations with dispersion. And finally, the main results of this report are summarized in Section 9 and the details of the numerical methods used to integrate the NLCME with dispersion and the MLE are given in the Appendixes A and B.

2 Maxwell-Lorentz equations

We describe the propagation of light in a fiber with a periodic grating and a cubic nonlinearity using the one-dimensional Maxwell's equations [4, 5] for the electromagnetic fields evolution together with an anharmonic Lorentz oscillator model for the polarization (see e.g. [6, 7] and references therein),

$$\frac{\partial B}{\partial t} = \frac{\partial E}{\partial x}, \quad (1)$$

$$\mu_0 \frac{\partial D}{\partial t} = \frac{\partial B}{\partial x}, \quad (2)$$

$$D = \epsilon_0 E + P, \quad (3)$$

$$\Omega_p^{-2} \frac{\partial^2 P}{\partial t^2} + (1 - 2\Delta n \cos(2\pi x/\lambda_g))P - \gamma P^3 = \epsilon_0 \chi E. \quad (4)$$

In the system above, the electric field E , the magnetic field B , the dielectric displacement D and the polarization P are scalar fields that depend on the spatial variable x and on time t . μ_0 and ϵ_0 denote, respectively, the permeability and the permittivity of the vacuum. The characteristic frequency Ω_p accounts for the non instantaneous polarization response of the media, Δn and λ_g represent the strength and the period of the grating, that is, the strength and the period of the spatial periodic variation of the refractive index of the fiber (Δn measures the size of the nonuniformities of the refraction index relative to its mean value n_0 , see Fig. 1), χ is the linear polarizability of the medium ($n_0^2 = 1 + \chi$) and $\gamma > 0$ is the coefficient of the nonlinear Kerr effect.

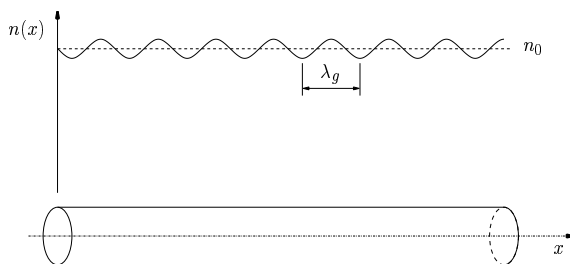


Figure 1: One dimensional fiber with periodic variation of the refractive index.

In order to simplify subsequent calculations it is convenient to make the system

(1)-(4) non dimensional using the following rescalings:

$$B = \sqrt{\mu_0/(\epsilon_0\gamma)}\tilde{B}, \quad D = (1/\sqrt{\gamma})\tilde{D}, \quad E = (1/\sqrt{(\epsilon_0\gamma)})\tilde{E}, \quad P = (1/\sqrt{\gamma})\tilde{P},$$

$$x = (\lambda_g/\pi)\tilde{x}, \quad t = (\lambda_g/c\pi)\tilde{t},$$

here $c^2 = 1/(\epsilon_0\mu_0)$ is the vacuum speed of light. After dropping tildes, the non-dimensional Maxwell-Lorentz equations (MLE hereafter) can be written as

$$\frac{\partial B}{\partial t} = \frac{\partial E}{\partial x}, \tag{5}$$

$$\frac{\partial D}{\partial t} = \frac{\partial B}{\partial x}, \tag{6}$$

$$D = E + P, \tag{7}$$

$$\omega_p^{-2} \frac{\partial^2 P}{\partial t^2} + (1 - 2\Delta n \cos(2x))P - P^3 = (n_0^2 - 1)E, \tag{8}$$

where the dimensionless finite time polarization response frequency is now $\omega_p^2 = \Omega_p^2 \lambda_g^2 / (c^2 \pi^2)$. Notice that we have rescaled the spatial variable x to make wavenumber of the grating equal to 2 (see eq. (8)). As we will see below, the reason for this choice is that the wavetrains that resonate with the grating and develop along the fiber will then have wavenumber 1. We have also used the rescaling to absorb the vacuum properties ϵ_0 and μ_0 (the vacuum speed of light is now equal to 1 in the rescaled variables) and the nonlinear coefficient γ . As a result, the MLE above depend only on three dimensionless parameters: ω_p^2 , Δn and n_0^2 .

We are interested in the description of the solutions of the MLE in the physically relevant regime of small grating strength (i.e., near uniform refractive index fiber) and small nonlinear Kerr effect, that is,

$$|\Delta n| \ll 1 \quad \text{and} \quad |E|, |B|, |D|, |P| \ll 1.$$

To achieve this goal we need to understand first the linear light propagation characteristics in a uniform fiber. The next step, the weakly nonlinear analysis of the light propagation in a nearly uniform fiber that is performed in the next section, is just a small perturbation of this basic configuration of uniform fiber without nonlinear effects.

This linear analysis is carried out by looking for uniform wavetrain solutions with

spatial wavenumber k and frequency ω_k ,

$$\begin{pmatrix} E(x, t) \\ B(x, t) \\ D(x, t) \\ P(x, t) \end{pmatrix} = \begin{pmatrix} E_k \\ B_k \\ D_k \\ P_k \end{pmatrix} e^{ikx+i\omega_k t} + \text{c.c.}, \quad (9)$$

in the linearized version of the MLE without grating $\Delta n = 0$ (here c.c. stands for the complex conjugate). This produces the following algebraic eigenvalue problem

$$\begin{aligned} \omega_k B_k &= k E_k \\ \omega_k D_k &= k B_k \\ D_k &= E_k + P_k \\ (1 - \omega_k^2/\omega_p^2) P_k &= \chi E_k \end{aligned}$$

that has nontrivial solutions if and only if ω_k satisfies the following fourth order polynomial equation,

$$\omega_k^4 - \omega_k^2(k^2 + \omega_p^2 n_0^2) + \omega_p^2 k^2 = 0, \quad (10)$$

which, for $n_0^2 > 1$ [4, 5, 8], has four real roots of the form

$$\omega_k = \pm \sqrt{(k^2 + \omega_p^2 n_0^2)/2 \pm \sqrt{(k^2 + \omega_p^2 n_0^2)^2/4 - \omega_p^2 k^2}}, \quad (11)$$

with associated eigenvectors,

$$\begin{pmatrix} E_k \\ B_k \\ D_k \\ P_k \end{pmatrix} = \begin{pmatrix} \omega_k^2 \\ k\omega_k \\ k^2 \\ k^2 - \omega_k^2 \end{pmatrix} \quad (12)$$

The four branches of the dispersion relation (11) are plotted in Fig. 2. The $k \rightarrow -k$ symmetry of ω_k comes from the invariance of the MLE without grating ($\Delta n = 0$) under spatial reflections $x \rightarrow -x$, and the $\omega_k \rightarrow -\omega_k$ symmetry is due to the fact that the MLE are also invariant under reflection in time $t \rightarrow -t$ (time reversal symmetry). For every wavenumber k there are four possible propagative wavetrains of the form given in eq. (9), and the corresponding wavetrains with

wavenumbers $-k$ are the complex conjugates.

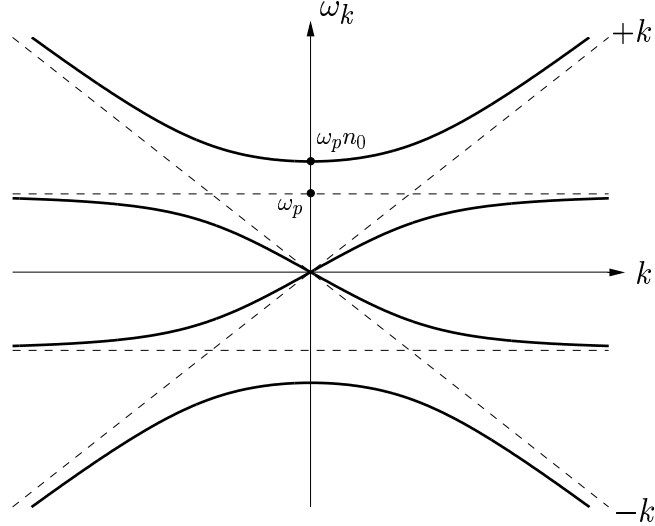


Figure 2: Sketch of the dispersion relation (11).

It is interesting to notice that the two branches of ω_k that remain in between $+k$ and $-k$ correspond to wavetrains with polarization in phase with the electric field, i.e., $k^2 - \omega_k^2 > 0$ in (12), while for the other two branches the fields are in opposite phase. There are also two very different behaviors for large wavenumbers: one is dominated by the finite time polarization response of the medium, $\omega_k \rightarrow \pm\omega_p$ as $k \rightarrow \pm\infty$, and the other, $\omega_k \rightarrow \pm k$ as $k \rightarrow \pm\infty$, corresponds to propagation like in the vacuum, without polarization effects.

3 Envelope equation description

In this section we derive, from the MLE (5)-(8), the envelope equations that describe the weakly nonlinear propagation of light wavepackets in a fiber with periodic variation of the refractive index.

The small nonuniformities of the refractive index, $\Delta n \ll 1$, and the effect of the small nonlinearity, $|B|, |D|, |P|, |E| \ll 1$, can be accounted for by allowing the linear wavetrains obtained in the previous section (9) to be slowly modulated in space and time

$$\begin{pmatrix} E(x, t) \\ B(x, t) \\ D(x, t) \\ P(x, t) \end{pmatrix} = \begin{pmatrix} E_k \\ B_k \\ D_k \\ P_k \end{pmatrix} A(x, t) e^{ikx+i\omega_k t} + \text{c.c.} + \dots \quad (13)$$

Here A is the small amplitude of the wavetrain whose temporal and spatial variations take place in a much longer scale than that of the basic wavetrain (which is assumed to be of order one, i.e., $k \sim 1$ and $\omega_k \sim 1$). The expression above represents a wavepacket composed of modes with wavenumbers in a narrow band around k and frequencies near ω_k . Using standard multiple scales techniques, a single amplitude equation (or envelope equation) can be obtained for the slow evolution of the amplitude of the envelope of the wavetrain $A(x, t)$. This kind of derivation for nonlinear optics problems can be found in, e.g. [6, 7, 8], and in the review [9] for more general pattern forming phenomena in physical systems of different nature. The method used to derive the amplitude equations can be summarized as follows: insert the expansion (13) into the MLE (5)-(8) and force the resonant terms to cancel at every order to ensure that the solution remain bounded in the short time scale; the desired amplitude equation is precisely this cancellation condition.

If we take (13) into the MLE (5)-(8), then the first order contribution of the grating term is proportional to

$$2\Delta n \cos(2x)(Ae^{ikx+i\omega_k t} + \text{c.c.}) = \Delta n(e^{i2x} + e^{-i2x})(Ae^{ikx+i\omega_k t} + \text{c.c.}). \quad (14)$$

The expression above is composed of wavepackets with frequencies $\pm\omega_k$ and wavenumbers $\pm k \pm 2$, and gives rise to resonant terms (i.e., wavetrains that satisfy the dispersion relation (11)) only for $k = \pm 1$ (see Fig. 2). Therefore, as anticipated in the

previous section, only those wavepackets (13) with wavenumber and frequency

$$k = \pm 1 \quad \text{and} \quad \omega_k = \omega = \sqrt{(1 + \omega_p^2 n_0^2)/2 \pm \sqrt{(1 + \omega_p^2 n_0^2)^2/4 - \omega_p^2}} \quad (15)$$

are affected by the grating. The effect of the grating manifests itself as a spatial resonance that couples both wavepackets: the wavepacket with $k = 1$ produces a resonant term with wavenumber $k = -1$ and the same frequency and vice versa (see eq. (14)). Wavepackets with wavenumber $k \neq \pm 1$ do not feel the grating in first approximation, they propagate like in a uniform fiber and the weakly nonlinear evolution of its amplitude is then given by the standard nonlinear Schrödinger equation, see e.g. [4, 5, 7, 8].

In the remaining part of this section we derive the amplitude equations for the weakly nonlinear evolution of two resonantly interacting wavepackets with wavenumbers close to $k = \pm 1$.

We first eliminate the dielectric displacement D and the magnetic field B from the MLE (5)-(8), and rewrite them as a system of two second order partial differential equations for the polarization P and the electric field E ,

$$\frac{\partial^2(E + P)}{\partial t^2} = \frac{\partial^2 E}{\partial x^2}, \quad (16)$$

$$\frac{\partial^2 P}{\partial t^2} = -\omega_p^2(1 - 2\Delta n \cos(2x))P + \omega_p^2(n_0^2 - 1)E + \omega_p^2 P^3. \quad (17)$$

And we then look for solutions of the system above that are composed, at first order, of two counterpropagating, slowly modulated wavetrains with wavenumbers $k = \pm 1$ and frequency ω (15)

$$\begin{Bmatrix} E(x, t) \\ P(x, t) \end{Bmatrix} = V_0(A^+(x, t)e^{ix+i\omega t} + A^-(x, t)e^{-ix+i\omega t}) + \text{c.c.} + \dots, \quad (18)$$

where, according to (12), the eigenvector V_0 is given by

$$V_0 = \begin{Bmatrix} \omega^2 \\ 1 - \omega^2 \end{Bmatrix},$$

and the weakly nonlinear level of this approach requires essentially that

$$\dots \ll |A_{xx}^\pm| \ll |A_x^\pm| \ll |A^\pm| \ll 1, \quad \dots \ll |A_t^\pm| \ll |A^\pm| \ll 1 \quad \text{and} \quad \Delta n \ll 1, \quad (19)$$

that is, small amplitudes that depend slowly on space and time and small grating strength.

The appropriate expansions for the solution of eqs. (16)-(17) and the amplitude equations in powers of the small quantities Δn , A^\pm , A_x^\pm , A_{xx}^\pm , ... (which will be treated here as independent parameters) are thus of the form

$$\begin{aligned} \left\{ \begin{array}{l} E(x, t) \\ P(x, t) \end{array} \right\} &= V_0(A^+ e^{ix+i\omega t} + A^- e^{-ix+i\omega t}) + \text{c.c.} + \\ &\quad + v_1^+ A_x^+ + v_1^- A_x^- + v_2^+ A_{xx}^+ + v_2^- A_{xx}^- + \dots, \end{aligned} \quad (20)$$

$$A_t^+ = \alpha_0^+ A^+ + \alpha_1^+ A_x^+ + \alpha_2^+ A_{xx}^+ + \dots, \quad (21)$$

$$A_t^- = \alpha_0^- A^- + \alpha_1^- A_x^- + \alpha_2^- A_{xx}^- + \dots \quad (22)$$

Inserting the expansions above into eqs. (16)-(17), a linear nonhomogeneous system is obtained for the contribution of each order. For the resonant terms, i.e., those proportional to $e^{\pm ix \pm i\omega t}$, a condition must be satisfied to ensure that there are not secular terms in the short scale. In other words, the linear problems corresponding to the resonant terms are singular and hence a solvability condition must be satisfied by the nonhomogeneous part; these solvability conditions give the coefficients of the amplitude equations.

Notice that only the resonant terms contribute to the amplitude equations and only the amplitude equation for A^+ has to be calculated because the corresponding equation for A^- can be obtained by simply applying the symmetry

$$x \rightarrow -x \quad A^+ \longleftrightarrow A^-, \quad (23)$$

which comes from the spatial reflection symmetry of the original problem (5)-(8).

The linear terms in the amplitude equations can be easily anticipated because they correspond to the Taylor expansion of the dispersion relation (11) at $k = 1$ (see e.g. [9]),

$$i(\omega_k|_{k=1} - \omega)A^+ + \left. \frac{d\omega_k}{dk} \right|_{k=1} A_x^+ - i \frac{1}{2} \left. \frac{d^2\omega_k}{dk^2} \right|_{k=1} A_{xx}^+ + \dots$$

The first coefficient vanishes (see eq. (15)) and the second and third coefficients are, respectively, the group velocity and the material dispersion, and, after making use of eq. (10), can be written as

$$v_g = \left. \frac{d\omega_k}{dk} \right|_{k=1} = \frac{\omega(\omega^2 - \omega_p^2)}{\omega^4 - \omega_p^2}, \quad (24)$$

$$id = -i \frac{1}{2} \left. \frac{d^2\omega_k}{dk^2} \right|_{k=1} = -i \frac{1}{2} \frac{\omega^3(\omega^2 - 1)(\omega^2 - \omega_p^2)(3\omega_p^2 + \omega^4)}{(\omega^4 - \omega_p^2)^3}. \quad (25)$$

The first order, resonant contributions of the grating to the expansion of the solution (18) and to the amplitude equation (21) are of the form

$$W \Delta n A^- e^{ix+i\omega t} \quad \text{and} \quad w \Delta n A^-,$$

where the two component vector W is given by the following linear, singular non-homogeneous problem

$$\begin{bmatrix} \omega^2 - 1 & \omega^2 \\ (n_0^2 - 1)\omega_p^2 & \omega^2 - \omega_p^2 \end{bmatrix} W = -\omega_p^2 \begin{bmatrix} 0 & 0 \\ 0 & 1 \end{bmatrix} V_0 + 2i\omega w \begin{bmatrix} 1 & 1 \\ 0 & 1 \end{bmatrix} V_0.$$

This system can be solved only if the right hand side is orthogonal to the solution of the adjoint problem

$$V_0^a = \left\{ \begin{array}{c} \omega_p^2 - \omega^2 \\ \omega^2 \end{array} \right\}.$$

This solvability condition gives the value of the coefficient of the amplitude equation

$$w = i \frac{\omega(1 - \omega^2)}{2(\omega^4 - \omega_p^2)} \omega_p^2. \quad (26)$$

The first order contributions of the nonlinear term,

$$U_1 A^+ |A^+|^2 e^{ix+i\omega t}, \quad U_2 A^+ |A^-|^2 e^{ix+i\omega t} \quad \text{and} \quad u_1 A^+ |A^+|^2, \quad u_2 A^+ |A^-|^2,$$

are computed similarly. The following linear problems are obtained for the vectors

U_1 and U_2

$$\begin{aligned} \begin{bmatrix} \omega^2 - 1 & \omega^2 \\ (n_0^2 - 1)\omega_p^2 & \omega^2 - \omega_p^2 \end{bmatrix} U_1 &= -3\omega_p^2 \begin{bmatrix} 0 \\ (1 - \omega^2)^3 \end{bmatrix} + 2i\omega u_1 \begin{bmatrix} 1 & 1 \\ 0 & 1 \end{bmatrix} V_0, \\ \begin{bmatrix} \omega^2 - 1 & \omega^2 \\ (n_0^2 - 1)\omega_p^2 & \omega^2 - \omega_p^2 \end{bmatrix} U_2 &= -6\omega_p^2 \begin{bmatrix} 0 \\ (1 - \omega^2)^3 \end{bmatrix} + 2i\omega u_2 \begin{bmatrix} 1 & 1 \\ 0 & 1 \end{bmatrix} V_0, \end{aligned}$$

and, after applying the solvability condition, the resulting amplitude equation coefficients are given by

$$u_1 = i \frac{3\omega(1 - \omega^2)^3}{2(\omega^4 - \omega_p^2)} \omega_p^2 \quad \text{and} \quad u_2 = i \frac{3\omega(1 - \omega^2)^3}{(\omega^4 - \omega_p^2)} \omega_p^2. \quad (27)$$

Collecting the coefficients above (24)-(27) and applying the spatial reflection symmetry (23) the amplitude equations can be finally written as

$$A_t^+ = v_g A_x^+ + idA_{xx}^+ + w\Delta n A^- + A^+(u_1|A^+|^2 + u_2|A^-|^2) + \dots, \quad (28)$$

$$A_t^- = -v_g A_x^- + idA_{xx}^- + w\Delta n A^+ + A^-(u_1|A^-|^2 + u_2|A^+|^2) + \dots \quad (29)$$

Notice that the grating and nonlinear coefficients (26),(27) are purely imaginary. This result could have been anticipated without any calculations because the amplitude equations have to be invariant under the transformation

$$t \rightarrow -t \quad A^\pm \rightarrow \overline{A^\mp}, \quad (30)$$

that comes from the time reversal ($t \rightarrow -t$) invariance of the MLE (16),(17). Also, the fact that the only nonlinearity in the MLE is cubic forces the nonlinear coefficients (27) to verify

$$u_2 = 2u_1.$$

We will consider the simplest possible geometrical configuration: propagation of light in a fiber ring with length $L \gg 1$. The spatial periodicity condition for the electric field and the polarization implies that the boundary conditions for A^+ and A^- are (see eq. (18))

$$A^+(x + L)e^{i\theta} = A^+(x, t), \quad A^-(x + L)e^{-i\theta} = A^-(x, t). \quad (31)$$

Here $\theta = L \pmod{2\pi}$ measures the mismatch between the natural wavelength of the wavepackets ($=2\pi$) and the period of the domain, but we will restrict our analysis to the particular case $\theta = 0$ (i.e., ring length equals to an integer multiple of the basic period of the wavepackets) to reduce the number of parameters of the problem.

There are two possible choices for ω (ω^\pm) depending on the sign selected in (15), see Fig. 3. As mentioned in the previous section, these two possibilities correspond to a configuration with the electric field and the polarization in phase (for $\omega = \omega^-$) and in opposite phase (for $\omega = \omega^+$). The group velocity (24) is positive in both cases (it is the slope of the curve ω_k at $k = 1$ in Fig. 3) but the sign of the material dispersion coefficient d (25), which is related to the curvature of the curve ω_k in Fig. 3, changes. The nonlinear and grating terms have imaginary parts that are always negative; see eqs. (26) and (27) and Fig. 3, and recall that, using the dispersion relation (10) for $k = 1$, the denominator can be written as $\omega^4 - \omega_p^2 = \omega^2[(\omega^2 - 1) + (\omega^2 - \omega_p^2)n_0^2]$.

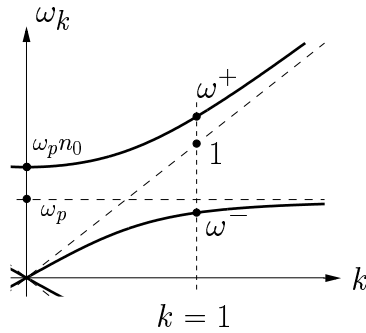


Figure 3: Detail of the dispersion relation (11) with the two frequencies ω^\pm for $k = 1$.

In order to make the nonlinear and grating coefficients positive, we will work with the complex conjugates of the amplitudes and, to absorb some of the parameters of the problem, we will also perform the following rescalings

$$x = L\tilde{x}, \quad t = (L/v_g)\tilde{t}, \quad \bar{A}^\pm = \sqrt{v_g/(L|u_2|)}\tilde{A}^\pm, \quad (32)$$

that, after dropping tildes, yield the scaled equations

$$A_t^+ = A_x^+ + i\varepsilon A_{xx}^+ + i\kappa A^- + iA^+(\sigma|A^+|^2 + |A^-|^2), \quad (33)$$

$$A_t^- = -A_x^- + i\varepsilon A_{xx}^- + i\kappa A^+ + iA^-(\sigma|A^-|^2 + |A^+|^2), \quad (34)$$

$$A^\pm(x+1, t) = A^\pm(x, t), \quad (35)$$

where $\varepsilon = -d/(Lv_g) \ll 1$ is positive (negative) for $\omega = \omega^+$ ($\omega = \omega^-$), the scaled grating strength $\kappa = \Delta nL|w|/v_g \sim 1$ is always positive, and the nonlinear coefficient $\sigma = \frac{1}{2}$.

If we neglect the material dispersion terms (i.e., set $\varepsilon = 0$) in the system above then the so-called nonlinear coupled mode equations (NLCME) are obtained,

$$A_t^+ - A_x^+ = i\kappa A^- + iA^+(\sigma|A^+|^2 + |A^-|^2), \quad (36)$$

$$A_t^- + A_x^- = i\kappa A^+ + iA^-(\sigma|A^-|^2 + |A^+|^2), \quad (37)$$

$$A^\pm(x+1, t) = A^\pm(x, t), \quad (38)$$

Equations (36)-(37) represent a balance of the transport at the group velocity, the effect of the grating and the Kerr nonlinearity. This hyperbolic system and its more remarkable solutions have been widely studied theoretically and numerically, see e.g. [10, 11, 2, 6, 12, 13, 15, 16, 17, 18, 19, 20, 14]. Also, some interesting generalizations of the NLCME have been recently analyzed, including dual core fibers and quadratic nonlinearities [3], stimulated Brillouin scattering [21] and nonlinear effects in the grating strength [22, 23]. And similar hyperbolic systems have been used for the description of Bose-Einstein condensates [24] and spontaneous Hopf bifurcations in dissipative pattern forming systems [25, 26, 27].

The purpose of this research project is to study the effect of the addition of small dispersive terms to the solutions of the NLCME, that is, to analyze the system (33)-(35) in the limit $\varepsilon \rightarrow 0$. There are some recent papers [28, 29, 30] that study the NLCME with dispersive terms but they do not cover the physically relevant regime: small dispersion coefficient.

The small dispersive terms of the system (33)-(35) constitute a singular perturbation of the NLCME and introduce a new small dispersive scale $l_d \sim \sqrt{|\varepsilon|} \ll 1$. The solutions of the NLCME are approximated solutions (up to $\mathcal{O}(\varepsilon)$ errors) of the system with small dispersion (33)-(35). Our goal is to determine which solutions of

the NLCME remain stable in the system with small dispersion and which ones are unstable against perturbations containing small dispersive scales. For the solutions that develop dispersive scales the dynamics predicted by the NLCME is not correct and the complete system with dispersion must be integrated. Similar analyses can be found in [27] in the context of the oscillatory instability in dissipative systems, and in [31] for the onset of the Faraday instability in a nearly conservative system.

The next sections are dedicated to the study the effect of the small dispersion in a well known family of solutions of the NLCME, namely, the continuous wave solutions.

4 Continuous wave solutions

The simplest solutions of the NLCME (36)-(38) are the so-called continuous wave fields (CW) that correspond to amplitudes with steady, uniform modulus (see [17] and [20]). These solutions are of the form

$$A^+ = A_{cw}^+ = \rho \cos \theta e^{i\alpha t + imx}, \quad (39)$$

$$A^- = A_{cw}^- = \rho \sin \theta e^{i\alpha t + imx}, \quad (40)$$

where $\rho \geq 0$ and $\theta \in [-\frac{\pi}{2}, \frac{\pi}{2}]$, and the frequency and wavenumber of the amplitudes are given by

$$\alpha = \frac{\kappa}{\sin 2\theta} + \frac{\sigma + 1}{2} \rho^2, \quad (41)$$

$$m = \left(\frac{\kappa}{\sin 2\theta} - \frac{\sigma - 1}{2} \rho^2 \right) \cos 2\theta. \quad (42)$$

The corresponding physical fields (see eq. (18)) are the superposition of two uniform counterpropagating wavetrains, and m and α represent, respectively, small corrections to the basic wavetrains wavenumber and frequency. To be more precise, the resulting wavenumbers and frequencies of the wavetrains in eq. (18) are $1 \pm \frac{m}{L}$ and $\omega + \frac{\alpha}{L} v_g$, with $L \gg 1$. The parameter ρ represents the total power propagating along the fiber,

$$\rho^2 = |A_{cw}^+|^2 + |A_{cw}^-|^2,$$

and θ measures the ratio between the two wavetrains. For $\theta = \pm \frac{\pi}{4}$ both amplitudes have the same size and the physical fields take the form of a standing wave, while for $\theta \rightarrow 0$ and $\theta \rightarrow \pm \frac{\pi}{2}$ one of the amplitudes vanishes and the pattern inside the fiber is a pure travelling wave.

In the linear limit of small light intensity ($\rho = 0$) the relation between the CW wavenumber, m , and frequency, α , is given by

$$m^2 = \alpha^2 \left(1 - \frac{\kappa^2}{\alpha^2} \right),$$

which is plotted in Fig. 4. It is clear from this figure that the main effect of the grating in the linear light propagation characteristics (discussed at the end of Section 2, see Fig. 2) is to open a frequency gap of size 2κ , centered at the resonant

point $(m, \alpha) = (0, 0)$, i.e., $(k, \omega_k) = (1, \omega)$ in terms of the original variables (9), for which there is no possible propagation. This opening of a “photonic band gap” of excluded frequencies is a typical resonance effect in wave propagation problems in linear periodic media. For the linear modes with wavenumbers near $m = 0$ (θ close to $\pm\frac{\pi}{4}$ in eqs. (41) and (42), see Fig. 4) the reflection produced by the grating is maximum and when we move away from the resonance point ($\theta \rightarrow 0$ and $\theta \rightarrow \pm\frac{\pi}{2}$) the effect of the grating is gradually reduced and the linear propagation characteristics of bare fiber ($\alpha = \pm m$, in our scaled variables) are recovered.

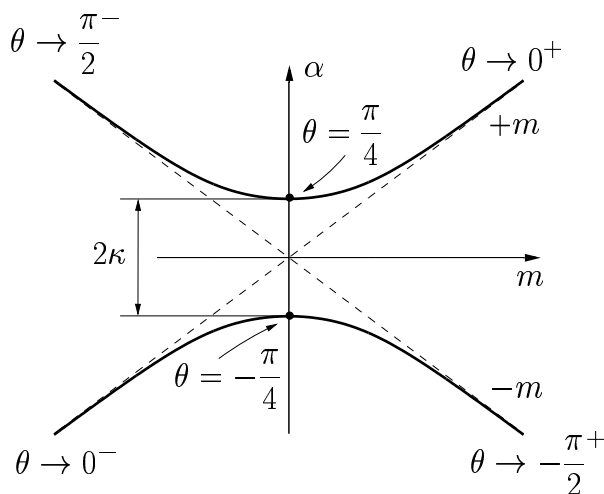


Figure 4: Linear light propagation characteristics in a fiber grating showing the frequency gap.

As the power is increased, $\rho > 0$, the effect of the nonlinearity of the fiber comes into play and the relation between the frequency and the wavenumber of the CW becomes more complicated,

$$m^2 = (\alpha - \sigma\rho^2)^2 \left(1 - \frac{\kappa^2}{(\alpha - (\frac{1+\sigma}{2})\rho^2)^2}\right).$$

The equation above is a fourth order polynomial equation in α and it does not have real solutions if

$$\left|\alpha - \left(\frac{1+\sigma}{2}\right)\rho^2\right| \leq \kappa,$$

hence the frequency gap remains of size 2κ and it is just shifted upwards by the nonlinear effects. The structure of the CW is essentially similar to that of the linear

case, i.e., there are two CW with for every wavenumber m , if the power is below the critical value

$$\rho_c = \sqrt{\frac{2\kappa}{|1-\sigma|}},$$

see Fig. 5a, while for $\rho > \rho_c$ the nonlinear distortion becomes more important and a region of higher multiplicity of CW solutions (up to 4) develops near $m = 0$ (see Fig. 5b).

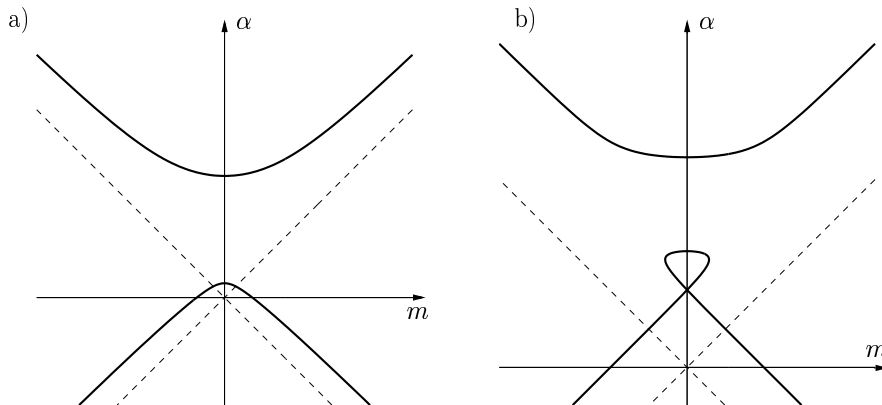


Figure 5: $\alpha - m$ plot of the CW with constant power ρ for a) $\rho < \rho_c$ and b) $\rho > \rho_c$ ($\sigma = \frac{1}{2}$).

We conclude the description of the CW introducing the representation of this family of solutions in the (θ, ρ^2) plane, shown in Fig. 6. This is a convenient way to represent the CW because each point on the (θ, ρ^2) plane corresponds to a single CW and vice versa, and there are not multiple solutions. In Fig. 6, white (shaded) regions correspond to positive (negative) wavenumber, and the thick lines are the $m = 0$ curves, that are given by, see (42),

$$\rho^2 = \rho_x^2 = -\frac{2\kappa}{(1-\sigma)\sin(2\theta)} \quad \text{and} \quad \theta = \pm\frac{\pi}{4}. \quad (43)$$

The CW inside the region $\rho^2 > \rho_x^2$ in Fig. 6 correspond to those that lie along the loop that appears for $\rho > \rho_c$ in the $\alpha - m$ plots of the CW, see Fig. 5b. Constant m ($m \neq 0$) lines are plotted in Fig. 6 as thin lines with arrows indicating the m growing direction (recall that $m \rightarrow \pm\infty$ for $\theta \rightarrow 0$ and $\theta \rightarrow \pm\frac{\pi}{2}$, see eq. (42)). Note that the only allowed values of the wavenumber m are those compatible with the

periodicity boundary conditions (38), i.e., those of the form

$$m = 2\pi n, \quad \text{with } n \in \mathbb{Z}.$$

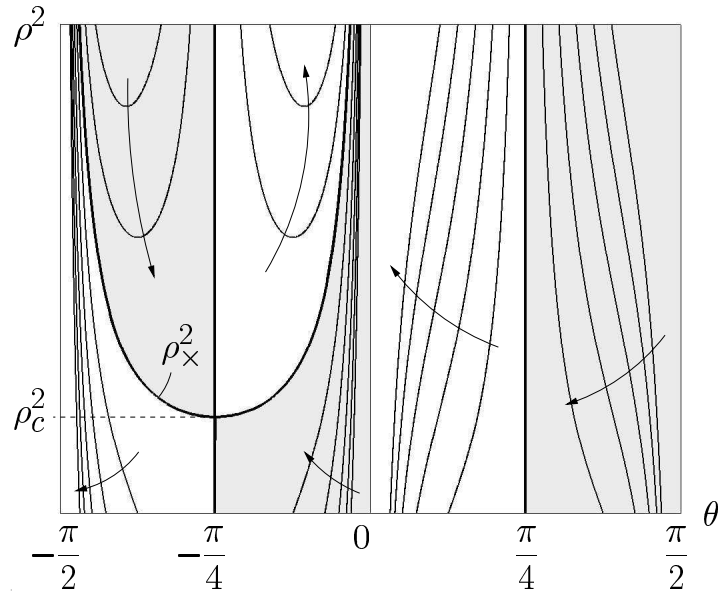


Figure 6: The (θ, ρ^2) representation of the CW ($\sigma = \frac{1}{2}$).

It is interesting to notice also that this (θ, ρ^2) representation is somewhat redundant because the CW corresponding to θ and that corresponding to $\pm\frac{\pi}{2} - \theta$ are the same after a spatial reflection (23). This results in the symmetry around $\theta = \pm\frac{\pi}{4}$ that can be appreciated in Fig. 6.

5 Stability of the CW

The linear stability characteristics of the family of continuous wave (CW) solutions (39)-(40) are obtained in this section. This is performed in two steps: we will first study the stability of the CW against perturbations with wavenumber of order unity (this completes the analysis presented in [17]), and we will then use the NLCME with small dispersion terms (33)-(35) to compute the stability of the perturbations that contain small dispersive scales.

The evolution of the infinitesimal perturbations of the CW, defined by

$$A^+ = A_{cw}^+(1 + a^+), \quad A^- = A_{cw}^-(1 + a^-), \quad \text{with } |a^\pm| \ll 1,$$

is given by the linearized version of equations (33)-(35)

$$\begin{aligned} a_t^+ - a_x^+ &= i\kappa(a^- - a^+) \tan \theta + i\sigma\rho^2 \cos^2 \theta(a^+ + \overline{a^+}) + i\rho^2 \sin^2 \theta(a^- + \overline{a^-}) + i\varepsilon a_{xx}^+, \\ a_t^- + a_x^- &= i\kappa(a^+ - a^-) / \tan \theta + i\sigma\rho^2 \sin^2 \theta(a^- + \overline{a^-}) + i\rho^2 \cos^2 \theta(a^+ + \overline{a^+}) + i\varepsilon a_{xx}^-, \\ a^\pm(x+1, t) &= a^\pm(x, t). \end{aligned}$$

This linear system is solved via the Fourier expansion

$$(a^+, a^-) = \sum_{k=-\infty}^{\infty} (a_k^+(t), a_k^-(t)) e^{i2\pi kx},$$

where k represents the spatial wavenumber of the perturbation and the coefficients a_k^\pm satisfy the following system of ordinary differential equations

$$\begin{aligned} \frac{da_k^+}{dt} &= i(2\pi k)a_k^+ + i\kappa(a_k^- - a_k^+) \tan \theta + i\sigma\rho^2 \cos^2 \theta(a_k^+ + \overline{a_{-k}^+}) \\ &\quad + i\rho^2 \sin^2 \theta(a_k^- + \overline{a_{-k}^-}) - i\varepsilon(2\pi k)^2 a_k^+, \end{aligned} \quad (44)$$

$$\begin{aligned} \frac{da_k^-}{dt} &= -i(2\pi k)a_k^- + i\kappa(a_k^+ - a_k^-) / \tan \theta + i\sigma\rho^2 \sin^2 \theta(a_k^- + \overline{a_{-k}^-}) \\ &\quad + i\rho^2 \cos^2 \theta(a_k^+ + \overline{a_{-k}^+}) - i\varepsilon(2\pi k)^2 a_k^-. \end{aligned} \quad (45)$$

The small parameter ε in the system above allows us to distinguish between two essentially different types of perturbations that are studied separately: perturbations with ($k \sim (1/\sqrt{|\varepsilon|}) \gg 1$) and without ($k \sim 1$) small dispersive scales.

5.1 Perturbations with $k \sim 1$ wavenumber

In this case the dispersive terms in eqs. (44)-(45) are small and can be neglected. The resulting equations together with those corresponding to $\overline{a_{-k}^{\pm}}$ form a quartet that is uncoupled from the equations for the other wavenumbers. If we look for solutions of this quartet proportional to $e^{\Omega t}$, the following fourth order polynomial equation for Ω is obtained

$$(\Omega^2 + (2\pi k)^2)^2 + 2\kappa^2(\Omega^2 + (2\pi k)^2) + 4\kappa\rho^2 \frac{\tan\theta}{1 + \tan^2\theta} ((2\pi k)^2(1 + \sigma) + \Omega^2(1 - \sigma)) + \kappa^2 \tan^2\theta (\Omega + i(2\pi k))^2 + \frac{\kappa^2}{\tan^2\theta} (\Omega - i(2\pi k))^2 = 0,$$

that can be turned into a real coefficient polynomial equation by means of the change of variable $\Omega = i\omega$

$$(\omega^2 - (2\pi k)^2)^2 - 2\kappa^2(\omega^2 - (2\pi k)^2) + 4\kappa\rho^2 \frac{\tan\theta}{1 + \tan^2\theta} ((2\pi k)^2(1 + \sigma) - \omega^2(1 - \sigma)) - \kappa^2 \tan^2\theta (\omega + (2\pi k))^2 - \frac{\kappa^2}{\tan^2\theta} (\omega - (2\pi k))^2 = 0. \quad (46)$$

For the particular case of uniform perturbations, $k = 0$, the solutions of (46) can be calculated explicitly

$$\omega = 0 \text{ (double)} \quad \text{and} \\ \omega = \pm \sqrt{\frac{4\kappa^2}{\sin^2(2\theta)} + 2\kappa\rho^2(1 - \sigma) \sin(2\theta)},$$

and thus we have instability, i.e., Ω with positive real part, when

$$\rho^2 > \rho_0^2 = -\frac{2\kappa}{(1 - \sigma) \sin^3(2\theta)}. \quad (47)$$

This instability region lies inside the higher multiplicity region $\rho^2 > \rho_x^2$, see eq. (43), and is represented in Fig. 7. The condition above states that the CW that correspond to the upper part of the loop represented in Fig. 5b are unstable. This can be easily seen from expression (42): the vertical slope points in the α versus m curve in Fig. 5b are given by the condition $\frac{\partial m}{\partial \theta} = 0$ that is equivalent to $\rho^2 = \rho_0^2$.

In the limit of large wavenumbers, $k \rightarrow \pm\infty$, the solutions of eq. (46) can be

expanded as

$$\omega = \omega_0 + \omega_1 + \dots, \quad \text{with} \quad |\omega_0| \gg |\omega_1| \gg \dots$$

The first order term $\omega_0 \sim k \gg 1$ satisfies the equation

$$(\omega_0^2 - (2\pi k)^2)^2 = 0,$$

whose solutions are of the form $\omega_0 = \pm 2\pi k$ and correspond to purely imaginary values of Ω . In order to determine the stability of the CW we have to compute the next order correction $\omega_1 \sim 1$ that is given by

$$\omega_1^2 = \kappa^2 \tan^{\pm 2} \theta - 2\sigma\kappa\rho^2 \frac{\tan \theta}{1 + \tan^2 \theta}.$$

The CW are then unstable if the imaginary part of ω_1 is nonzero, and this occurs inside the region defined by the conditions

$$\rho^2 > \rho_\infty^2 = \frac{\kappa \tan^{\pm 2} \theta}{\sigma \sin(2\theta)}, \quad (48)$$

that is represented in Fig. 7. Notice that, for the CW in this region, all perturbations with wavenumber above a certain threshold are unstable. This instability affects only the upper branch of CW in Fig. 5a ($\theta > 0$) and if the power on the fiber is such that $\rho^2 > k/\sigma$ then all CW along this branch are unstable.

The stability analysis of the CW is completed with the determination of the unstable perturbations with finite nonzero wavenumber. These perturbations correspond to complex conjugate pairs of roots (with nonzero imaginary part) in eq. (46),

$$\omega = a \pm ib \quad (b \neq 0) \quad \implies \quad \Omega = \pm b + ia \quad \text{unstable.}$$

This task can be somewhat simplified by taking into account the invariance of eq. (46) under the transformations

$$(\omega, k) \rightarrow (-\omega, -k) \quad \text{and} \quad (\omega, \tan \theta) \rightarrow (-\omega, 1/\tan \theta)$$

that allows us to restrict the search to the parameter range

$$k > 0 \quad \text{and} \quad \theta \in \left[-\frac{\pi}{4}, \frac{\pi}{4}\right].$$

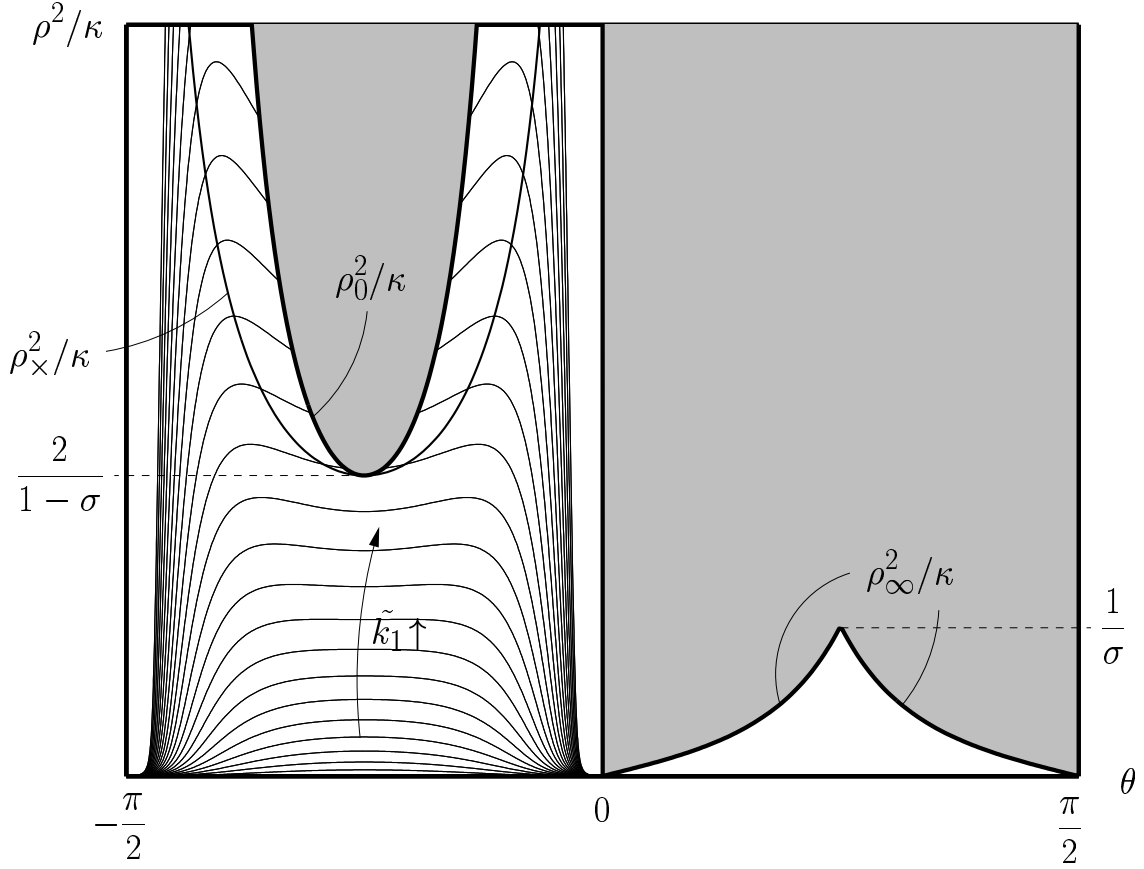


Figure 7: Stability properties of the CW for $\sigma = \frac{1}{2}$ (shading indicates instability). Thin solid lines correspond to $\tilde{k}_1 = 0.25 + 0.25n$, with $n = 0, 1, 2, \dots$. For a given value of κ , the CW above the line $\tilde{k}_1 = 2\pi/\kappa$ are unstable.

Furthermore, if we use the scaled variables

$$\tilde{\omega} = \omega/\kappa, \quad \tilde{k} = (2\pi k)/\kappa \quad \text{and} \quad \tilde{\rho}^2 = \rho^2/\kappa, \quad (49)$$

then the strength of the grating, $\kappa > 0$, can be absorbed and eq. (46) can be rewritten as

$$\begin{aligned} (\tilde{\omega}^2 - \tilde{k}^2)^2 - 2(\tilde{\omega}^2 - \tilde{k}^2) + 4\tilde{\rho}^2 \frac{\tan \theta}{1 + \tan^2 \theta} (\tilde{k}^2(1 + \sigma) - \tilde{\omega}^2(1 - \sigma)) \\ - \tan^2 \theta (\tilde{\omega} + \tilde{k})^2 - \frac{1}{\tan^2 \theta} (\tilde{\omega} - \tilde{k})^2 = 0. \end{aligned}$$

The onset of complex roots takes place when both the equation above and its derivative with respect to $\tilde{\omega}$ vanish. From these two equations the values of θ and $\tilde{\rho}^2$ are numerically computed for any given values of $\tilde{\omega}$ and \tilde{k} , and the following results are obtained:

- If $\theta > 0$ then there are no more instabilities apart from the one already obtained in the limit $k \rightarrow \pm\infty$ (48), see Fig. 7.
- For negative θ and for each value of $\tilde{\rho}^2 = \rho^2/\kappa$ there is a critical scaled wavenumber \tilde{k}_1 such that the perturbations with $\tilde{k} < \tilde{k}_1$ are unstable and those with $\tilde{k} > \tilde{k}_1$ are stable (the curves of constant \tilde{k}_1 value are plotted as thin solid lines in Fig. 7). A CW will be then unstable if the perturbation mode with lowest wavenumber ($k = 2\pi$) is unstable, that is, if

$$\frac{2\pi}{\kappa} < \tilde{k}_1, \quad (50)$$

see (49). Note that the previous instability boundaries (47) and (48) depend only on the combination of parameters ρ^2/κ , while the new instability defined by the condition above depends also on κ ; for a given value of κ , all the CW above the line $\tilde{k}_1 = 2\pi/\kappa$ are unstable, see Fig. 7.

- The CW near the $\rho^2 = \rho_0^2$ line present a small interval of stable scaled wavenumbers $\tilde{k} \in [0, \tilde{k}_2]$, but this does not modify the instability region defined above because, as it has been checked numerically, \tilde{k}_2 remains always below $\tilde{k}_1/2$.

Therefore, when we enter the region defined by condition (50) the CW become unstable against perturbations with wavenumber $k = \pm 1$, that is, with one single wavelength along the fiber. The lines of constant value of \tilde{k}_1 mark another instability limit for the CW, these lines move towards higher values ρ^2/κ as \tilde{k}_1 increases (see Fig.7) and they enter the higher multiplicity region $\rho^2 > \rho_x^2$, see eq. (43), at the critical value $\tilde{k}_{1c} = 2\sqrt{(1+\sigma)/(1-\sigma)}$.

We can summarize the results on this section as follows. The linear stability of the CW (without considering dispersion effects) is determined by the three conditions given by eqs. (47),(48) and (50), and, depending on the strength of the grating κ , we can have two different configurations that are sketched in Figs. 8 and 9. The CW with positive θ , i.e., those on the upper branch of the $\alpha - m$ representation in Fig. 5,

are always destabilized via the high wavenumber instability (48). While for negative θ the situation is more complicated: if $\kappa > \kappa_c = 2\pi/\tilde{k}_{1c} = \pi\sqrt{(1-\sigma)/(1+\sigma)}$ then the finite wavenumber instability (50) dominates (Fig. 8), but for $\kappa < \kappa_c$ the zero wavenumber instability (47) is also present and destabilizes the CW with θ near $-\pi/4$, see Fig. 9. Notice that for large values of the power in the grating ρ^2 all the CW are unstable and that, as the power is increased the first CW to become unstable are those that are close to pure TW, that is, those with θ near 0 or $\pm\pi/2$.

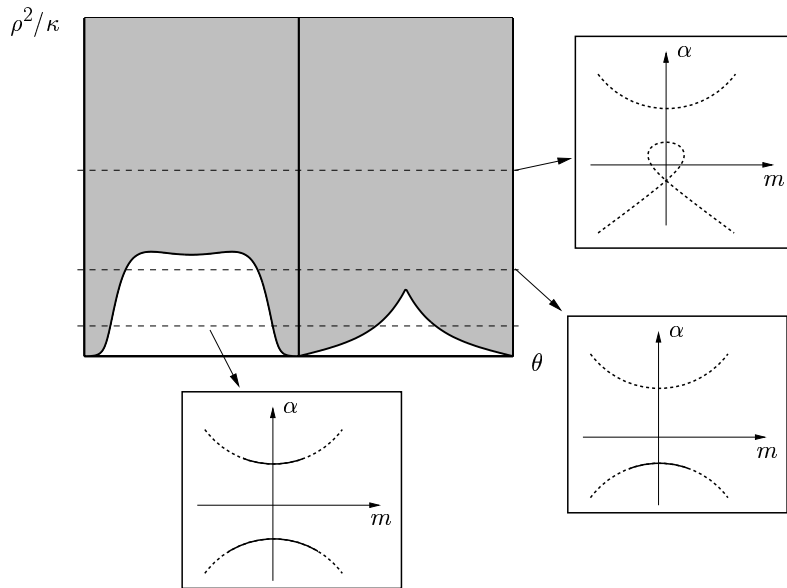


Figure 8: Stability properties of the CW for $\sigma = \frac{1}{2}$ and $\kappa > \kappa_c$ (shading indicates instability) together with the corresponding $\alpha - m$ plots (see Fig. 5) for several representative values of ρ^2 (solid and dashed lines indicate stable and unstable CW, resp.).

5.2 Perturbations with small dispersive scales

Figs. 8 and 9 summarize the stability properties of the CW in the context of the NLCME (36)-(38), that is, without small dispersion terms ($\varepsilon = 0$ in eqs. (33)-(35)). In the limit $\varepsilon \rightarrow 0$, the effect of the dispersion terms on the stability of the CW amounts to just a small correction of the results obtained in the previous section ($\varepsilon = 0$) for perturbations with wavenumber $k \sim 1$. This is not true for the perturbations with wavenumber on the dispersive scale, i.e. $|k| \sim 1/\sqrt{|\varepsilon|} \gg 1$ (see

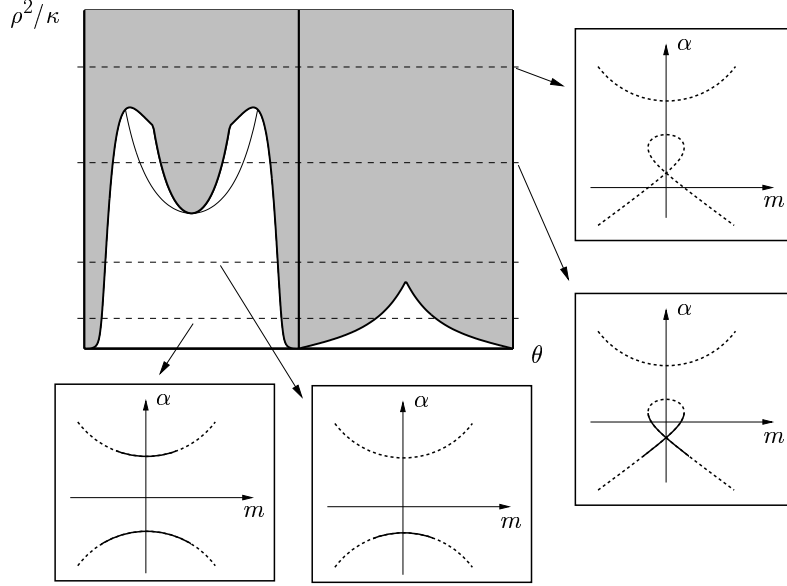


Figure 9: Stability properties of the CW for $\sigma = \frac{1}{2}$ and $\kappa < \kappa_c$ (shading indicates instability) together with the corresponding $\alpha - m$ plots (see Fig. 5) for several representative values of ρ^2 (solid and dashed lines indicate stable and unstable CW, resp.).

eqs. (44)-(45)). For these perturbations the dispersive terms must be retained and their stability characteristics can be calculated using multiple scales techniques.

To this end we define the scaled wavenumber $K = (2\pi k)\sqrt{|\varepsilon|} \sim 1$ and expand the solution of eqs. (44)-(45) in the form

$$a_K^+ = a_{K0}^+(t, T) + \sqrt{|\varepsilon|} a_{K1}^+(t, T) + \dots, \quad a_K^- = a_{K0}^-(t, T) + \sqrt{|\varepsilon|} a_{K1}^-(t, T) + \dots,$$

where $T = t/\sqrt{|\varepsilon|}$. At first order we obtain

$$\begin{aligned} \frac{da_{K0}^+}{dT} - iK a_{K0}^+ &= 0, \\ \frac{da_{K0}^-}{dT} + iK a_{K0}^- &= 0, \end{aligned}$$

whose general solution is given by

$$(a_{K0}^+, a_{K0}^-) = (A_{K0}^+(t)e^{iKT}, A_{K0}^-(t)e^{-iKT}).$$

Thus, in the fast time scale T , the group velocity term dominates and these short

wave, dispersive perturbations simply travel in opposite directions. At the next order we obtain

$$\begin{aligned}\frac{da_{K1}^+}{dT} - iKa_{K1}^+ &= \left[-\frac{dA_{K0}^+}{dt} - i\left(\kappa \tan \theta + \frac{\varepsilon}{|\varepsilon|}K^2\right)A_{K0}^+ + i\sigma\rho^2 \cos^2 \theta (A_{K0}^+ + \overline{A_{-K0}^+})\right]e^{iKT} \\ &\quad + [i\kappa \tan \theta A_{K0}^- + i\rho^2 \sin^2 \theta (A_{K0}^- + \overline{A_{-K0}^-})]e^{-iKT}, \\ \frac{da_{K1}^-}{dT} + iKa_{K1}^- &= \left[-\frac{dA_{K0}^-}{dt} - i\left(\kappa / \tan \theta + \frac{\varepsilon}{|\varepsilon|}K^2\right)A_{K0}^- + i\sigma\rho^2 \sin^2 \theta (A_{K0}^- + \overline{A_{-K0}^-})\right]e^{-iKT} \\ &\quad + [i\kappa / \tan \theta A_{K0}^+ + i\rho^2 \cos^2 \theta (A_{K0}^+ + \overline{A_{-K0}^+})]e^{iKT}.\end{aligned}$$

The higher order correction (a_{K1}^+, a_{K1}^-) will then remain bounded in the fast time scale T if the following equations are satisfied

$$\begin{aligned}\frac{dA_{K0}^+}{dt} &= -i\left(\kappa \tan \theta + \frac{\varepsilon}{|\varepsilon|}K^2\right)A_{K0}^+ + i\sigma\rho^2 \cos^2 \theta (A_{K0}^+ + \overline{A_{-K0}^+}), \\ \frac{dA_{K0}^-}{dt} &= -i\left(\kappa / \tan \theta + \frac{\varepsilon}{|\varepsilon|}K^2\right)A_{K0}^- + i\sigma\rho^2 \sin^2 \theta (A_{K0}^- + \overline{A_{-K0}^-}).\end{aligned}$$

These equations together with the corresponding ones for $(\overline{A_{-K0}^+}, \overline{A_{-K0}^-})$ form a linear system with constant coefficients that give the evolution the dispersive perturbations with wavenumber $\pm K$ in the slow time scale t . The left (+) and right (-) propagating perturbations (associated with the amplitudes A^+ and A^- , respectively) are uncoupled and their stability properties are given by the exponents

$$\Omega^+ = \pm \sqrt{\left(\kappa \tan \theta + \frac{\varepsilon}{|\varepsilon|}K^2\right)(2\sigma\rho^2 \cos^2 \theta - \left(\kappa \tan \theta + \frac{\varepsilon}{|\varepsilon|}K^2\right))}, \quad (51)$$

$$\Omega^- = \pm \sqrt{\left(\kappa / \tan \theta + \frac{\varepsilon}{|\varepsilon|}K^2\right)(2\sigma\rho^2 \sin^2 \theta - \left(\kappa / \tan \theta + \frac{\varepsilon}{|\varepsilon|}K^2\right))}, \quad (52)$$

and hence are unstable if the following conditions are satisfied

$$\begin{aligned}0 &\leq \kappa \tan \theta + \frac{\varepsilon}{|\varepsilon|}K^2 \leq 2\sigma\rho^2 \cos^2 \theta, \\ 0 &\leq \kappa / \tan \theta + \frac{\varepsilon}{|\varepsilon|}K^2 \leq 2\sigma\rho^2 \sin^2 \theta,\end{aligned}$$

that can be expressed as

$$\rho^2 \geq \rho_+^2 = \frac{\tan \theta}{\sigma \sin(2\theta)} (\kappa \tan \theta + \frac{\varepsilon}{|\varepsilon|} K^2) \quad \text{with} \quad \tan \theta \geq \frac{\varepsilon}{|\varepsilon|} \frac{K^2}{\kappa}, \quad \text{and} \quad (53)$$

$$\rho^2 \geq \rho_-^2 = \frac{\tan^{-1} \theta}{\sigma \sin(2\theta)} (\kappa \tan^{-1} \theta + \frac{\varepsilon}{|\varepsilon|} K^2) \quad \text{with} \quad \tan^{-1} \theta \geq \frac{\varepsilon}{|\varepsilon|} \frac{K^2}{\kappa}. \quad (54)$$

Notice that if we set $K^2 = 0$ then the instability condition (48) is recovered, in other words, the result for the limit $k \rightarrow \pm\infty$ in the $k \sim 1$ regime matches with the result for $K \rightarrow 0$ in the $k \sim 1/\sqrt{|\varepsilon|} \gg 1$ regime.

The above instability criterion define a family of regions in the $\theta - \rho^2$ plane, which depends on the parameter K^2 . The expression (53) is identical to (54) if we change $\tan \theta$ by $1/\tan \theta$, therefore it is enough to obtain the instability region defined by the ρ_+^2 condition; the corresponding one for ρ_-^2 is simply the symmetric around the vertical axes $\theta = \pm \frac{\pi}{4}$.

Fig. 10 shows these regions for $\varepsilon > 0$ and several values of $K^2 > 0$. A variation of the wavenumber from k to $k + 1$ results in a very small increment of $K \sim \sqrt{|\varepsilon|} \ll 1$, so, in first approximation, we allow K^2 to vary continuously in (53)-(54) and then the CW with negative θ ($\theta \in]-\frac{\pi}{2}, 0[$ in Fig. 10) are all rendered unstable. In exactly the same way, if $\varepsilon < 0$ then all the CW with positive θ are destabilized, see Fig. 11.

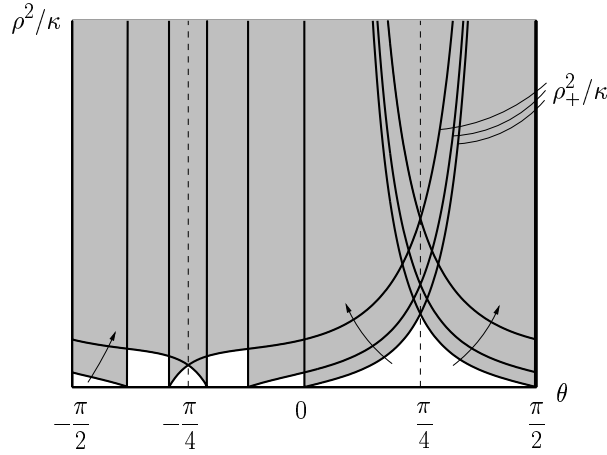


Figure 10: Dispersive instability conditions (53)-(54) for $\varepsilon > 0$, $\sigma = \frac{1}{2}$, and different values of K^2 (arrows point towards increasing K^2 direction and shading indicates instability).

Hence, the CW stability diagrams in Figs. 8 and 9 have to be complemented

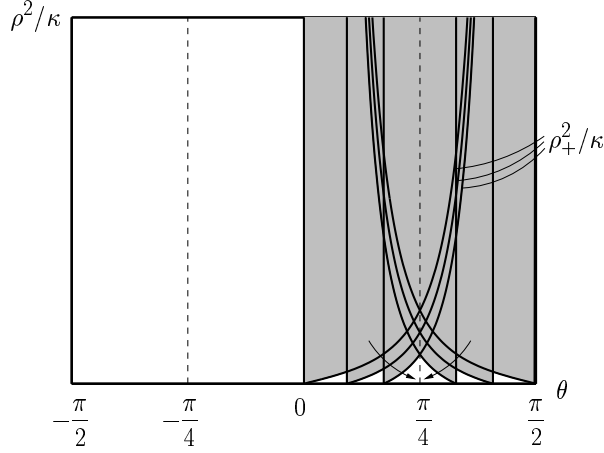


Figure 11: Dispersive instability conditions (53)-(54) for $\varepsilon < 0$, $\sigma = \frac{1}{2}$, and different values of K^2 (arrows point towards increasing K^2 direction and shading indicates instability).

with the following dispersive instability criterion:

$$- \text{for } \varepsilon > 0 \text{ (} \varepsilon < 0 \text{), all CW with } \theta < 0 \text{ (} \theta > 0 \text{) are unstable.} \quad (55)$$

In other words, the dispersive instability destabilizes all the CW along the lower (upper) branch in Fig. 5 if ε is positive (negative). And thus, for a given power inside the fiber ρ , there can be bistability only for $\rho > \rho_c$, $\kappa < \kappa_c$ and $\varepsilon < 0$ (see Fig. 9).

The small dispersion terms have a dramatic effect in the stability of the CW and they should not be ignored. The dispersive instability is not a higher order effect that appears in a much larger time scale; its growth rate is of order unity (and remains of order unity as $\varepsilon \rightarrow 0$, see eqs. (51)-(52)) and it develops in the transport time scale ($t \sim 1$) destabilizing small scales with typical size $\sqrt{|\varepsilon|} \ll 1$. Notice also that, in the limit $\varepsilon \rightarrow 0$, the dispersive instability condition (55) depends only on the sign of the dispersion coefficient (relative to the nonlinear coefficients) and it is present for both signs. For the CW with power higher than ρ_∞ , the beginning of the destabilization of the intermediate scales can be seen from the $k \rightarrow \infty$ limit of the stability analysis without dispersion (see Fig. 7), but for all other CW this instability is not detected if the dispersive terms are not taken into account, and the use of the NLCME eqs. (36)-(37) would therefore lead us to wrong conclusions.

5.3 Numerical simulations of the amplitude equations

In the following, we perform several numerical integrations of the NLCME equations with small dispersive terms (33)-(35) in order to check the CW stability boundaries obtained in the previous sections. The details of the numerical method can be found in Appendix A.

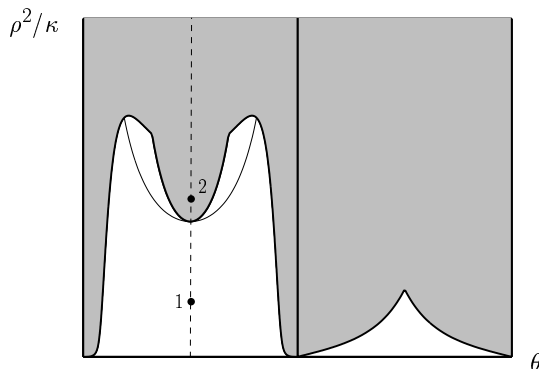


Figure 12: Stability properties of the CW (dispersive instabilities not shown) for $\sigma = \frac{1}{2}$ and $\kappa = 1$, shading indicates instability and dots correspond to the cases 1 and 2 CW.

We begin with the case 1 CW that corresponds to the parameter values $\sigma = \frac{1}{2}$, $\kappa = 1$, $\rho^2 = 1$ and $\theta = -\frac{\pi}{4}$ and, according to eqs. (41),(42), has wavenumber $m = 0$ and frequency $\alpha = -0.25$. The reconstructed original physical fields (see eq. (18)) produced by this spatially uniform CW take the form of a standing wave pattern along the fiber. As it can be seen in Fig. 12, the only source of instability for this CW is the dispersive instability: if $\varepsilon < 0$ then the perturbations containing small dispersive scales are stable and unstable otherwise. This is corroborated by the results of the numerical simulations of the amplitude equations (33)-(35) presented in Figs. 13 and 14, where we plot the time evolution of the norm of the amplitudes,

$$\|A\| = \sqrt{\int_0^1 |A|^2 dx},$$

for negative and positive dispersion, respectively, starting from the case 1 CW with a small perturbation. For negative dispersion the case 1 CW is stable and the small initial perturbations do not grow (Fig. 13). The perturbations cannot decay to zero because of the absence of dissipation in the system, and thus the value of the

spatial derivatives remains finite but small (comparable to the size of the initial perturbation, see Fig. 13). In contrast, if the dispersion is positive, the case 1 CW is unstable due to the exponential amplification of the small dispersive scales (see Fig. 14). This growth is not a slow time effect, it takes place in the time scale $t \sim 1$ and remains constant as $\varepsilon \rightarrow 0$, as it can be seen in the lower plot in Fig. 14, where we have added for comparison the time evolution of the spatial derivatives for two smaller dispersion values. The solution that develops consists of two counter-propagating wavetrains with dispersive wavelength ($\sim \sqrt{\varepsilon}$) and is shown in Fig. 15; notice how the number of peaks is approximately doubled when the dispersion is divided by 4.

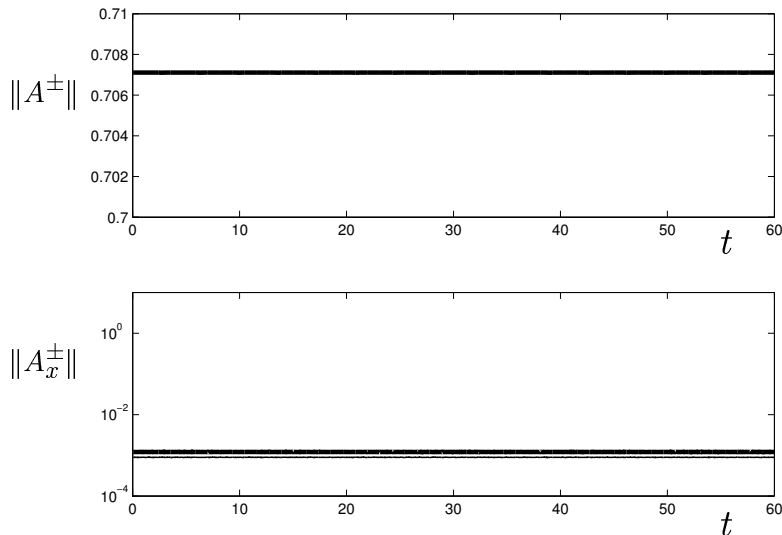


Figure 13: Thick (thin) lines indicate the time evolution of the spatial norm of A^+ (A^-) and its spatial derivative, for $\sigma = \frac{1}{2}$, $\kappa = 1$ and dispersion $\varepsilon = -10^{-3}$. The initial condition is the case 1 CW with a random perturbation of size $\sim 10^{-3}$.

In order to check the zero wavenumber stability boundary (47) we have numerically integrated the amplitude equations (33)-(35) starting from the case 2 CW ($\sigma = \frac{1}{2}$, $\kappa = 1$, $\rho^2 = 4.5$, $\theta = -\frac{\pi}{4}$, $m = 0$ and $\alpha = 2.375$, see Fig. 12) with a small random perturbation and negative dispersion, i.e., without dispersive instabilities. Fig. 16 shows the resulting solution. The small values of the spatial derivatives indicate that, as predicted by the linear stability theory, the destabilizing perturbation mode is the uniform one ($k = 0$). Moreover, the solution appears to remain almost

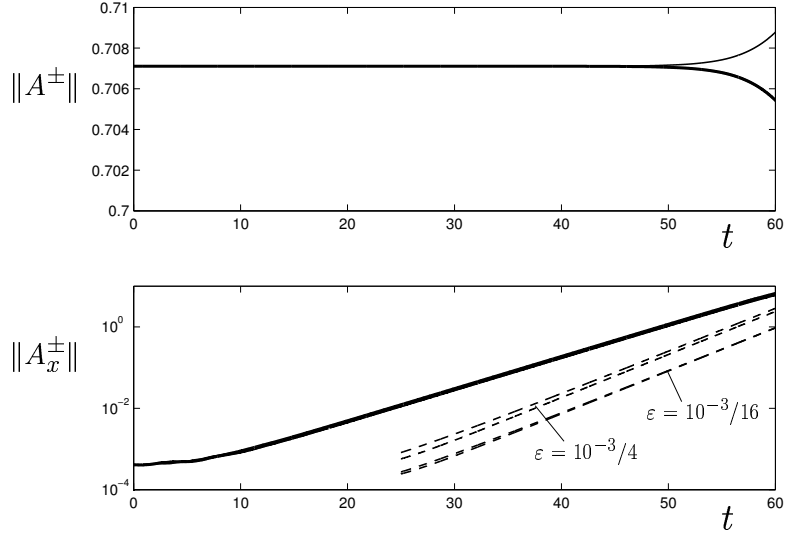


Figure 14: Thick (thin) lines indicate the time evolution of the spatial norm of A^+ (A^-) and its spatial derivative, for $\sigma = \frac{1}{2}$, $\kappa = 1$ and dispersion $\varepsilon = 10^{-3}$ (dashed lines correspond to smaller dispersion values). The initial condition is the case 1 CW with a small random perturbation of size $\sim 10^{-3}$.

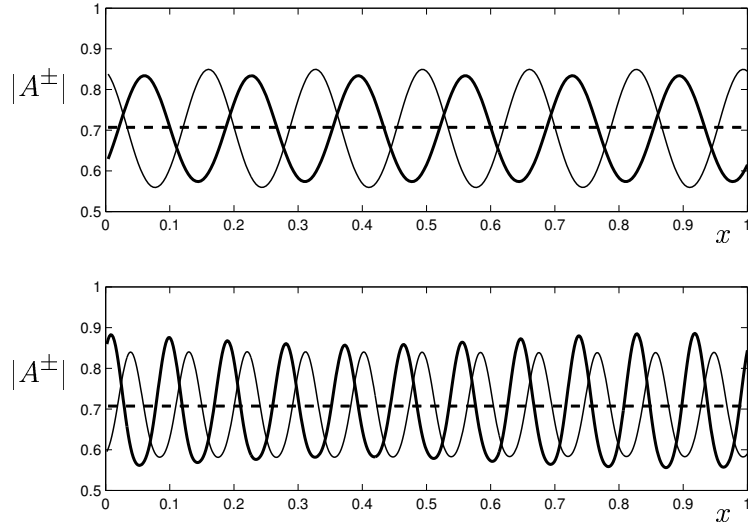


Figure 15: Snapshots of the solution of the amplitude equations (33)-(35) at $t = 60$ ($|A^+|$:thick line, $|A^-|$:thin line), with parameters as in Fig. 14 and dispersion $\varepsilon = 10^{-3}$ (above) and $\varepsilon = 10^{-3}/4$ (below).

uniform for all times and oscillates periodically between two states: one with both amplitudes nearly equal (close to a SW in the original physical variables) and other with A^+ dominating over A^- (close to a TW). Note that eqs. (33)-(35) preserve the total energy of the system, i.e.,

$$\frac{d}{dt} \int_0^1 (|A^+|^2 + |A^-|^2) dx = 0,$$

and therefore if the norm of one of the amplitudes increases the other has to decrease.

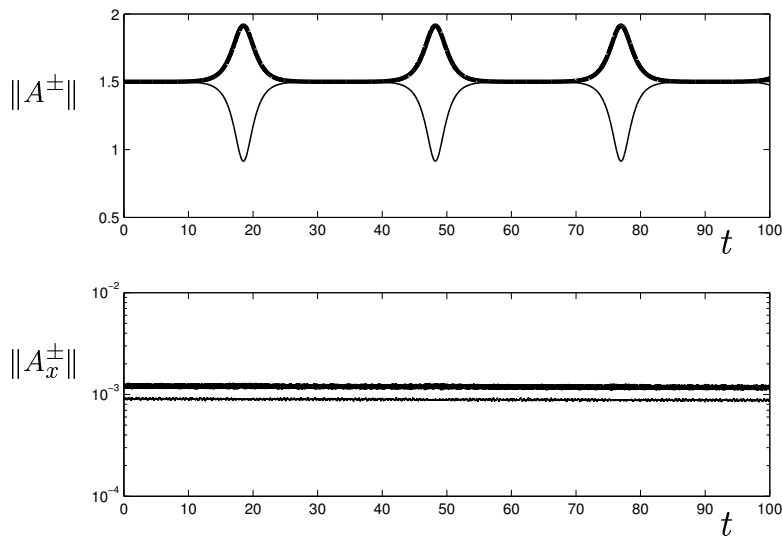


Figure 16: Thick (thin) lines indicate the time evolution of the spatial norm of A^+ (A^-) and its spatial derivative, for $\sigma = \frac{1}{2}$, $\kappa = 1$ and dispersion $\varepsilon = -10^{-3}$. The initial condition is the case 2 CW with a random perturbation of size $\sim 10^{-3}$.

In the case 3 CW ($\sigma = \frac{1}{2}$, $\kappa = 2$, $\rho^2 = 7.2$, $\theta = -\frac{\pi}{4}$, $m = 0$ and $\alpha = 3.4$), if the dispersion coefficient is kept negative, the destabilization is due only to condition (50), see Fig. 17. The time evolution of the solution of the amplitude eqs. (33)-(35) starting from the perturbed case 3 CW with $\varepsilon = -10^{-3}$ is shown in Fig. 18. The norms of the amplitudes are almost constant during the integration time, but the growth of the derivatives clearly indicates the onset of the instability that takes the system away from the starting uniform CW solution. The perturbation mode that destabilizes the CW is that with $k = 1$, i.e., that exhibiting one single wavelength inside the domain (see Fig. 19), in agreement with the linear stability

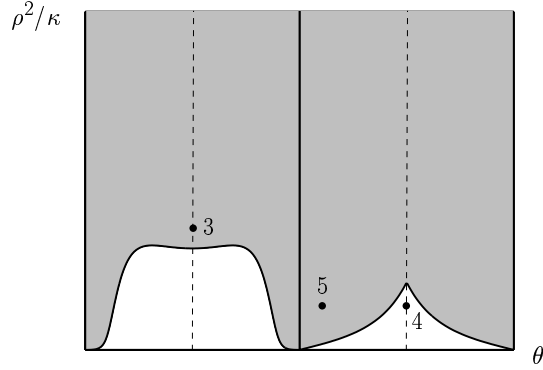


Figure 17: Stability properties of the CW (dispersive instabilities not shown) for $\sigma = \frac{1}{2}$ and $\kappa = 2$, shading indicates instability and dots correspond to the cases 3, 4 and 5 CW.

theory predictions.

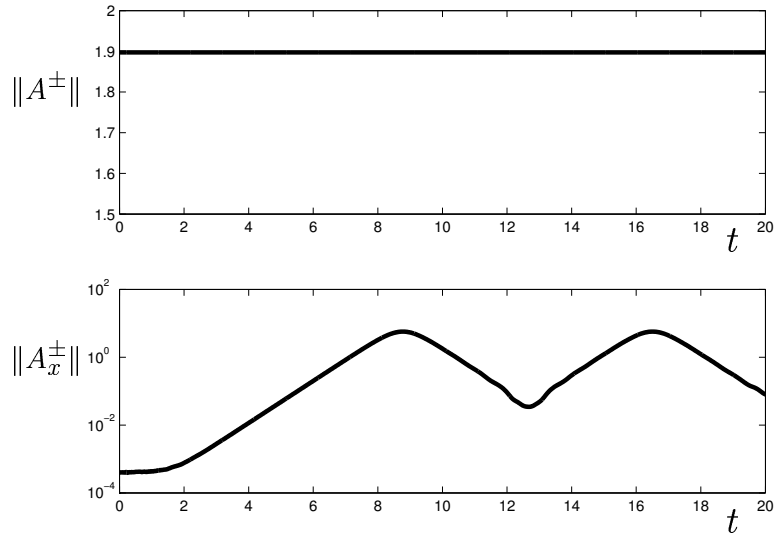


Figure 18: Thick (thin) lines indicate the time evolution of the spatial norm of A^+ (A^-) and its spatial derivative, for $\sigma = \frac{1}{2}$, $\kappa = 2$ and dispersion $\varepsilon = -10^{-3}$. The initial condition is the case 3 CW with a random perturbation of size $\sim 10^{-3}$.

For the case 4 CW ($\sigma = \frac{1}{2}$, $\kappa = 2$, $\rho^2 = 2$, $\theta = \frac{\pi}{4}$, $m = 0$ and $\alpha = 3.5$, see Fig. 17) the situation is the opposite of that of the case 1 CW. Now the CW is stable for positive values of the dispersion, as it can be observed in the numerical simulations represented in Fig. 20, and the dispersive instability develops, producing

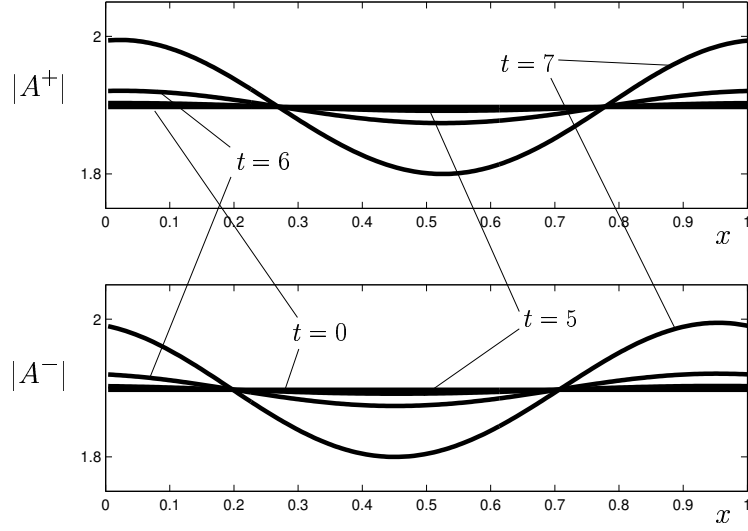


Figure 19: Spatial profiles of the solution of the amplitude equations (33)-(35) at times $t = 0, 5, 6$ and 7 , with all parameters as in Fig. 18.

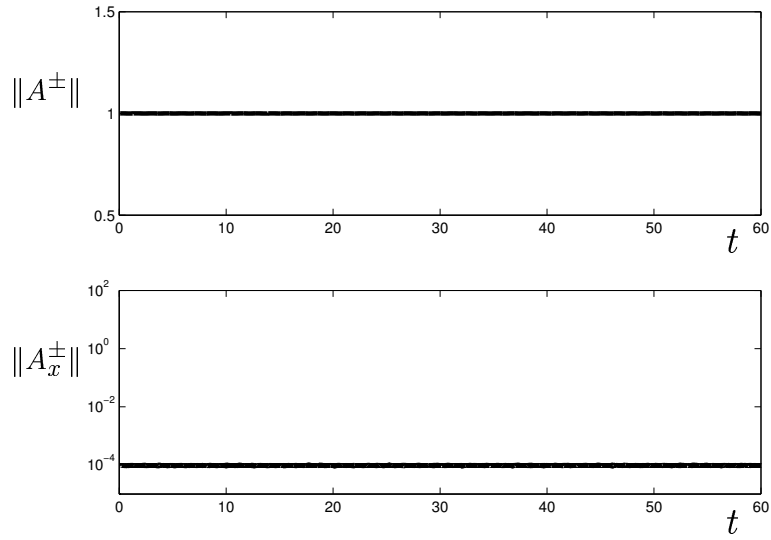


Figure 20: Thick (thin) lines indicate the time evolution of the spatial norm of A^+ (A^-) and its spatial derivative, for $\sigma = \frac{1}{2}$, $\kappa = 2$ and dispersion $\varepsilon = 10^{-3}$. The initial condition is the case 4 CW with a random perturbation of size $\sim 10^{-3}$.

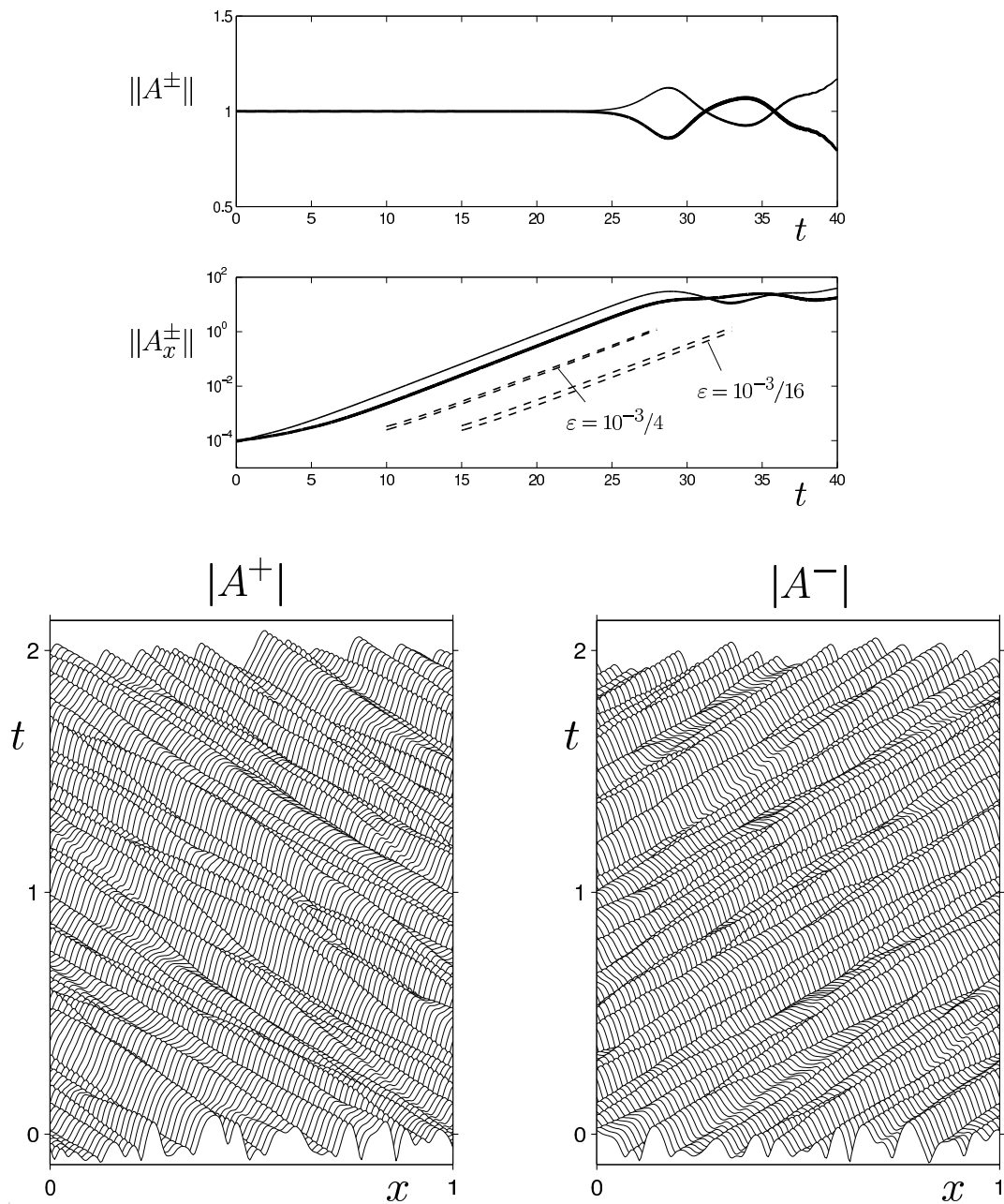


Figure 21: Top: thick (thin) lines indicate the time evolution of the spatial norm of A^+ (A^-) and its spatial derivative, for $\sigma = \frac{1}{2}$, $\kappa = 2$ and dispersion $\varepsilon = -10^{-3}$ (dashed lines correspond to smaller dispersion values). The initial condition is the case 4 CW with a small random perturbation of size $\sim 10^{-3}$. Bottom: space-time representation of the solution for two time units after $t = 80$.

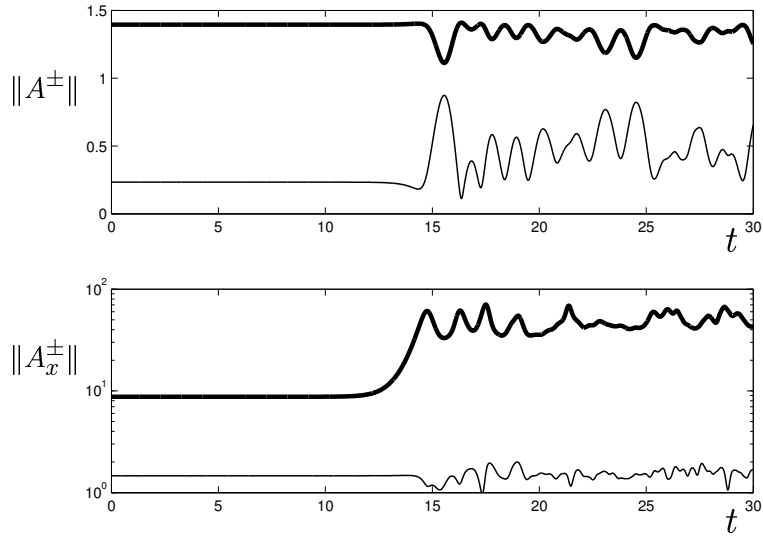


Figure 22: Thick (thin) lines indicate the time evolution of the spatial norm of A^+ (A^-) and its spatial derivative, for $\sigma = \frac{1}{2}$, $\kappa = 2$ and dispersion $\varepsilon = 10^{-3}$. The initial condition is the case 5 CW with a random perturbation of size $\sim 10^{-3}$.

small dispersive scales all over the domain, for negative dispersion (see Fig. 21). The time plot of $\|A_x^\pm\|$ in Fig. 21 shows the development of the dispersive instability for several dispersion values; note that, as predicted by the linear stability theory, the dispersive instability exponent tends to a nonzero constant as the dispersion coefficient is reduced $\varepsilon \rightarrow 0$. A space-time representation of the solution, once the dispersive scales are well developed, is also included in Fig. 21. Notice that the small dispersive scales are largely advected by the group velocity for short times, but they also evolve on a slower timescale, $t \sim 1$, to produce very complicated spatio-temporal dynamics. And notice also that the final state in terms of the original physical variables is even more complicated: it is the superposition of two faster counter-propagating wavetrains with amplitudes modulated by A^+ and A^- (see 18).

Finally, the case 5 CW ($\sigma = \frac{1}{2}$, $\kappa = 2$, $\rho^2 = 2$, $\theta = 0.1657$, $m = 1$ and $\alpha = 7.645$) is in the unstable side of condition (48), see Fig. 17. The numerical simulation shown in Fig. 22 indicates that, again in accordance with the linear stability results, the CW is unstable and the solution develops small dispersive scales. Notice that the growth rate of the perturbations is much larger for this case than for the previous ones. This is due to the fact that the extension of the

interval of unstable wavenumbers is now much longer: it starts in the $k \sim 1$ (48) region and extends up to the dispersive region $k \sim 1/\sqrt{|\varepsilon|}$ (see Figs. 10 and 11). Note also that the CW is inside the instability region that corresponds to the + sign in (48) and hence only the amplitude A^+ is unstable, as it can be seen in the initial growth of the derivative in the lower plot of Fig. 22.

6 Gap Solitons

Gap Solitons (GS) are solitary wave solutions of the NLCME (36)-(37) with temporal frequencies inside the frequency gap that opens up in the linear propagation characteristics of the grating, where uniform infinitesimal travelling wave states are not possible (see Fig. 4). These pulse-like solutions are the result of the combined effect of nonlinearity and grating reflection and have the property that they can propagate along the grating with any velocity between zero and the speed of light in the bare fibre. This is a very promising feature that gives the possibility (at least theoretically) to have localized packets of electromagnetic energy at zero or very low velocity in the laboratory frame.

This family of solutions, which are not true solitons since the NLCME with $\sigma \neq 0$ are not an integrable system, were introduced in [10, 11] and can be written in the form (see e.g. [13, 14, 6])

$$A_{GS}^+(x, t) = -\sqrt{\kappa}H(\xi) e^{-y/2+i\varphi(\xi)-i\kappa\gamma t} \quad (56)$$

$$A_{GS}^-(x, t) = \sqrt{\kappa}\bar{H}(\xi) e^{y/2+i\varphi(\xi)-i\kappa\gamma t} \quad (57)$$

where $\xi = \kappa(x - ct)$ is a moving spatial coordinate, c is the velocity of the GS

$$c = \tanh y, \quad \text{with } -\infty < y < +\infty, \quad (58)$$

$\kappa\gamma$ is its temporal frequency, with

$$\gamma = \cos \theta / \cosh y = \cos \theta \sqrt{1 - c^2}, \quad \text{with } 0 < \theta < \pi, \quad (59)$$

and the functions H and φ are given by

$$\varphi(\xi) = \frac{2\sigma \sinh(2y) \arctan\{\tan(\theta/2) \tanh[(\cosh y \sin \theta)\xi]\}}{1 + \sigma \cosh 2y} + (\sinh y \cos \theta)\xi, \quad (60)$$

$$H(\xi) = \frac{\sin \theta}{\sqrt{1 + \sigma \cosh 2y} \cosh[(\cosh y \sin \theta)\xi + i\theta/2]}. \quad (61)$$

Note that

$$H(-\xi) = \bar{H}(\xi), \quad \varphi(-\xi) = -\varphi(\xi), \quad (62)$$

and that $|H|$ reaches its maximum at $\xi = 0$ and then decays to zero monotonically

and exponentially fast as $\xi \rightarrow \pm\infty$.

The GS are solutions of the NLCME defined for $-\infty < x < \infty$ that correspond to localized pulses propagating with constant velocity c over a zero background and oscillating with frequency $\kappa\gamma$, like the one represented in Fig. 23.

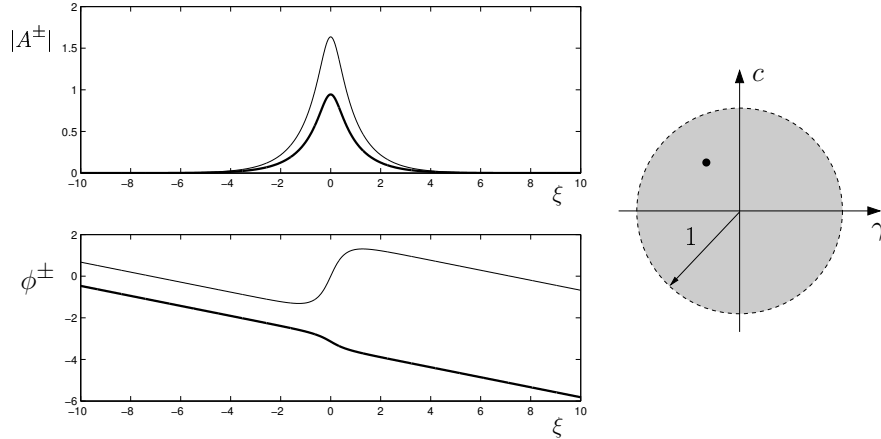


Figure 23: Left: Gap Soliton at $t = 0$, A^+ (A^-) thick (thin) line, with parameters $\sigma = \frac{1}{2}$, $\kappa = 1$, $c = \frac{1}{2}$ and $\theta = 2$. Right: domain of existence of the GS in the $c - \gamma$ plane (the dot corresponds to the GS shown).

For fixed values of σ and κ , this is a two parameter (y, θ) family of solutions with velocity and frequency in the ranges $-1 < c < 1$ and $-\sqrt{1-c^2} < \gamma < \sqrt{1-c^2}$, see eqs. (58) and (59). In the following we will represent the GS family in the $c - \gamma$ plane where it fills an open circle of radius one (Fig. 23). Notice also that the GS remain invariant under the changes $c \rightarrow -c$, $x \rightarrow -x$ and $A_{GS}^+ \leftrightarrow A_{GS}^-$ and therefore we can limit our analysis to the GS with $c \geq 0$.

7 Stability of the Gap Solitons

In this section we compute the linear stability characteristics of the GS in the context of the NLCME with small dispersion terms (33)-(34). We will proceed as we did in Section 5 with the CW: we will first study the stability of the GS against perturbations without dispersive scales, then the stability against dispersive perturbations and finally we will perform some numerical simulations to check the stability predictions.

Before starting with the stability calculations it is convenient to use the new space variable $\xi = \kappa(x - ct)$ to write the amplitude equations in a frame moving with the soliton and to eliminate the strength of the grating $\kappa > 0$ and the frequency of the soliton using the new time variable $\tau = \kappa t$ and the new amplitudes

$$A^\pm = \sqrt{\kappa} B^\pm \exp[-i\kappa\gamma t].$$

With all these changes the amplitude equations (33)-(34) take the form

$$B_\tau^+ - (c+1)B_\xi^+ = i\varepsilon\kappa B_{\xi\xi}^+ + i\gamma B^+ + iB^- + i(\sigma|B^+|^2 + |B^-|^2)B^+, \quad (63)$$

$$B_\tau^- - (c-1)B_\xi^- = i\varepsilon\kappa B_{\xi\xi}^- + i\gamma B^- + iB^+ + i(\sigma|B^-|^2 + |B^+|^2)B^-, \quad (64)$$

where $|\varepsilon| \ll 1$ and the GS (56),(57) are now steady states (up to first order corrections in ε)

$$B_{GS}^+ = -H(\xi)e^{-y/2+i\varphi(\xi)},$$

$$B_{GS}^- = \bar{H}(\xi)e^{y/2+i\varphi(\xi)}.$$

The linear stability of the GS is analyzed as usual, taking

$$B^\pm = B_{GS}^\pm + b^\pm, \quad \text{with } |b^\pm| \ll 1,$$

to eqs. (63)-(64) and linearizing, to obtain the system of equations

$$b_\tau^+ - (c+1)b_\xi^+ = i[\varepsilon\kappa b_{\xi\xi}^+ + (\gamma + \phi_1^+)b^+ + (1 + \phi_2)b^- + \phi_3^+\bar{b}^+ + \phi_4\bar{b}^-], \quad (65)$$

$$b_\tau^- - (c-1)b_\xi^- = i[\varepsilon\kappa b_{\xi\xi}^- + (\gamma + \phi_1^-)b^- + (1 + \bar{\phi}_2)b^+ + \phi_3^-\bar{b}^- + \phi_4\bar{b}^+], \quad (66)$$

with ξ -dependent coefficients that are given by

$$\phi_1^\pm(\xi) = 2\sigma|B_{GS}^\pm|^2 + |B_{GS}^\mp|^2 = (e^{\pm y} + 2\sigma e^{\mp y})|H(\xi)|^2 \quad (67)$$

$$\phi_2(\xi) = B_{GS}^\pm \bar{B}_{GS}^\mp = -H(\xi)^2, \quad (68)$$

$$\phi_3^+(\xi) = \sigma(B_{GS}^+)^2 = \sigma e^{-y+2i\varphi(\xi)} H(\xi)^2, \quad (69)$$

$$\phi_3^-(\xi) = \sigma(B_{GS}^-)^2 = \sigma e^{y+2i\varphi(\xi)} \bar{H}(\xi)^2, \quad (70)$$

$$\phi_4(\xi) = B_{GS}^+ B_{GS}^- = -e^{i2\varphi(\xi)} |H(\xi)|^2, \quad (71)$$

and verify (see (62))

$$\begin{aligned} \phi_1^\pm(-\xi) &= \bar{\phi}_1^\pm(\xi) = \phi_1^\pm(\xi), & \phi_2(-\xi) &= \bar{\phi}_2(\xi), \\ \phi_3^\pm(-\xi) &= \bar{\phi}_3^\pm(\xi), & \phi_4(-\xi) &= \bar{\phi}_4(\xi). \end{aligned}$$

7.1 Perturbations without dispersive scales

In this case, the perturbations exhibit only scales that remain $\xi \sim 1$ as $\varepsilon \rightarrow 0$. This allow us to neglect, in first approximation, the dispersion terms in the system (65)-(66), namely we set $\varepsilon = 0$ in eqs. (65)-(66). The resulting equations together with their complex conjugates form a linear system of four equations whose solutions can be written in the form

$$\begin{bmatrix} b^+ \\ b^- \\ \bar{b}^+ \\ \bar{b}^- \end{bmatrix} = \begin{bmatrix} X^+(\xi) \\ X^-(\xi) \\ Y^+(\xi) \\ Y^-(\xi) \end{bmatrix} e^{i\omega\tau}, \quad (72)$$

with ω and (X^\pm, Y^\pm) given by the following ODE eigenproblem

$$\omega X^+ + i(c+1)X_\xi^+ = (\gamma + \phi_1^+)X^+ + (1 + \phi_2)X^- + \phi_3^+Y^+ + \phi_4Y^-, \quad (73)$$

$$\omega X^- + i(c-1)X_\xi^- = (\gamma + \phi_1^-)X^- + (1 + \bar{\phi}_2)X^+ + \phi_3^-Y^- + \phi_4Y^+, \quad (74)$$

$$-\omega Y^+ - i(c+1)Y_\xi^+ = (\gamma + \phi_1^+)Y^+ + (1 + \bar{\phi}_2)Y^- + \bar{\phi}_3^+X^+ + \bar{\phi}_4X^-, \quad (75)$$

$$-\omega Y^- - i(c-1)Y_\xi^- = (\gamma + \phi_1^-)Y^- + (1 + \phi_2)Y^+ + \bar{\phi}_3^-X^- + \bar{\phi}_4X^+. \quad (76)$$

The spectrum of the problem above is composed of all $\omega \in \mathbb{C}$ with associated nonzero

eigenfunctions (X^\pm, Y^\pm) that remain bounded as $\xi \rightarrow \pm\infty$, either localized (point spectrum) or not (essential spectrum).

A GS is then unstable if there are values of ω in its spectrum with negative imaginary part. Note that the symmetries of eqs. (73)-(76)

$$(\omega, \xi, X^\pm, Y^\pm) \rightarrow (-\omega, -\xi, Y^\pm, X^\pm) \quad (77)$$

and

$$\omega \rightarrow -\bar{\omega}, \quad X^\pm \leftrightarrow \bar{Y}^\pm \quad (78)$$

allow us to restrict the analysis to

$$\Re\omega \geq 0 \quad \text{and} \quad \Im\omega \geq 0.$$

The first symmetry above follows from the spatial reflection (23) and time reversal (30) invariance of the system and the second is due to the particular form of the perturbation (72).

In the limit $|\xi| \rightarrow \infty$ the system (73)-(76) becomes a constant coefficient linear system and its solutions can be written in the form

$$(X^\pm, Y^\pm) = (X_0^\pm, Y_0^\pm)e^{i\alpha\xi}, \quad (79)$$

where the complex constants X_0^\pm, Y_0^\pm and α satisfy

$$[\gamma - \omega + (c + 1)\alpha]X_0^+ + X_0^- = 0, \quad (80)$$

$$[\gamma - \omega + (c - 1)\alpha]X_0^- + X_0^+ = 0, \quad (81)$$

and

$$[\gamma + \omega + (c + 1)\alpha]Y_0^+ + Y_0^- = 0, \quad (82)$$

$$[\gamma + \omega + (c - 1)\alpha]Y_0^- + Y_0^+ = 0. \quad (83)$$

Imposing that these systems exhibit nontrivial solutions, we obtain

$$(\gamma - \omega + c\alpha)^2 - \alpha^2 - 1 = 0 \quad (84)$$

for (80)-(81) and

$$(\gamma + \omega + c\alpha)^2 - \alpha^2 - 1 = 0 \quad (85)$$

for (82)-(83), and then for every value of ω we have, in general, four complex values of α that give the behavior of the eigenfunctions as $\xi \rightarrow \pm\infty$.

Real values of α correspond to eigenfunctions with oscillatory tails that remain bounded and do not decay to zero as $\xi \rightarrow \pm\infty$, see eq. (79). From eqs. (84) and (85), real values of α are seen to occur only for real values of ω along the four branches

$$\omega = c\alpha \pm \gamma \pm \sqrt{\alpha^2 + 1}, \quad \alpha \in \mathbb{R}.$$

This defines the essential spectrum of (73)-(76), which is confined to the real line and therefore it does not give rise to any instabilities. The essential spectrum is composed of four semi-infinite segments of the real line bounded by the four extrema of the expressions above: $\pm\omega_0$ and $\pm\omega_1$ (see Fig. 24), where $\omega_0 > 0$ and $\omega_1 > 0$ are given by

$$\omega_0 = -\gamma + \sqrt{1 - c^2} \quad \text{and} \quad \omega_1 = \gamma + \sqrt{1 - c^2}.$$

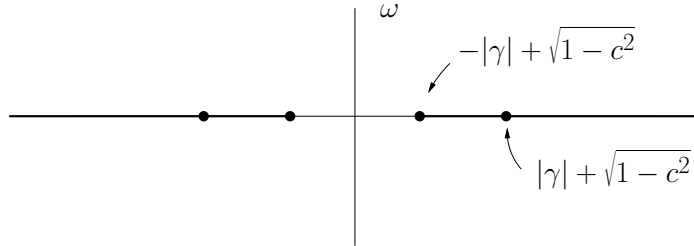


Figure 24: Essential spectrum in the complex ω plane (thick line) with dots marking its edges.

Away from the essential spectrum, the roots of eqs. (84) and (85),

$$\alpha_X^\pm = \frac{-c(\omega - \gamma) \pm \sqrt{(\omega - \gamma)^2 - (1 - c^2)}}{1 - c^2} \quad (86)$$

and

$$\alpha_Y^\pm = \frac{-c(\omega + \gamma) \pm \sqrt{(\omega + \gamma)^2 - (1 - c^2)}}{1 - c^2}, \quad (87)$$

respectively, have nonzero imaginary parts with opposite signs (the $+$ ($-$) super index corresponds to the root with positive (negative) imaginary part). This is

readily seen after taking into account that the imaginary parts of the roots α_X^\pm can be regarded as two real functions that depend continuously on ω , do not vanish in the connected set obtained after removing the essential spectrum from the complex plane (recall that the essential spectrum is precisely the set where $\Im\alpha = 0$) and have different signs at $\omega = 0$; and the same holds true for α_Y^\pm . In order to ensure that both $|X^\pm|$ and $|Y^\pm|$ remain bounded, we must remove the exponentially growing eigenfunctions, and the only allowed asymptotic behaviors as $\xi \rightarrow \pm\infty$ are

$$(X^+, X^-) = (-1, \gamma - \omega + (c + 1)\alpha_X^\pm) e^{i\alpha_X^\pm \xi}, \quad (88)$$

$$(Y^+, Y^-) = (-1, \gamma + \omega - (c + 1)\alpha_Y^\pm) e^{i\alpha_Y^\pm \xi}. \quad (89)$$

Summarizing, outside the essential spectrum, the eigenfunctions are given by (73)-(76) together with the boundary conditions (88) and (89).

The point spectrum is now calculated by means of the so-called Evans function, which is defined as follows (see e.g. [32, 33] and [34] for a recent review on this topic). For each $\omega \in \mathbb{C}$ outside the essential spectrum we integrate (73)-(76) both from $\xi \rightarrow -\infty$ and from $\xi \rightarrow +\infty$ and starting from a linear combination of (88) and (89), to obtain

$$(X_-^\pm, Y_-^\pm) = K_1(X_1^\pm, Y_1^\pm) + K_2(X_2^\pm, Y_2^\pm)$$

and

$$(X_+^\pm, Y_+^\pm) = K_3(X_3^\pm, Y_3^\pm) + K_4(X_4^\pm, Y_4^\pm),$$

respectively. Note that once the appropriate asymptotic behavior is imposed, each orbit depends linearly on two (complex) constants. These two orbits must have a non void intersection at $\xi = 0$, namely they must satisfy $(X_-^\pm, Y_-^\pm) = (X_+^\pm, Y_+^\pm)$ at $\xi = 0$. This is a homogeneous, fourth order linear system for K_1, \dots, K_4 and we define the Evans function, $E(\omega)$, as the value of the determinant its coefficient matrix. Therefore, it has nontrivial solutions if and only if

$$E(\omega) = 0.$$

In other words, the Evans function detects the intersections of the stable and unsta-

ble manifold of the fixed point $(X^\pm, Y^\pm) = (0, 0)$ of (73)-(76) and it is defined only when $(0, 0)$ is hyperbolic, that is, for ω values outside the essential spectrum. It is an analytic function, as it follows from the analyticity of the constituent solutions $(X_1^\pm, Y_1^\pm), \dots, (X_4^\pm, Y_4^\pm)$, with the property that its zeros coincide with the eigenvalues. Note that because of the symmetries (77) and (78) the Evans function must also be such that

$$E(-\omega) = E(\omega) \quad \text{and} \quad \overline{E(\omega)} = E(\bar{\omega}). \quad (90)$$

We can now analyze the stability of the GS just by applying the principle of the argument to the Evans function along the contour depicted in Fig. 25, which encircles the half complex plane that corresponds to ω with positive imaginary part, to obtain the number of unstable eigenvalues.

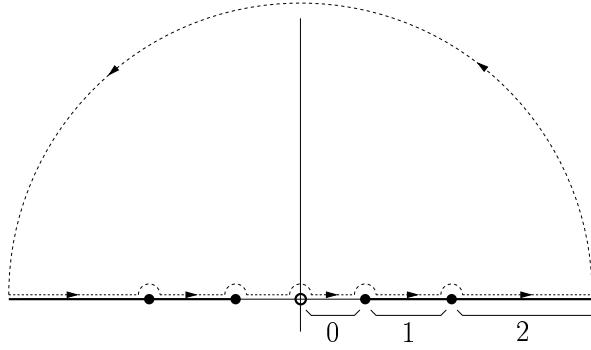


Figure 25: Contour in the complex ω plane for the application of the principle of the argument to $E(\omega)$. The thick line correspond to the essential spectrum and the black dots mark its edges.

In order to do this we have to take into account the following considerations:

- Using the analytic extension of the square roots in (86) and (87), we can extend analytically the Evans function from the half complex plane $\Im\omega > 0$ to the essential spectrum, except at its edges, $\pm\omega_0$ and $\pm\omega_1$, where the extended Evans function presents singularities. Note that the Evans function is not continuous at the essential spectrum and thus its extensions from above and below (namely, from $\Im\omega > 0$ and from $\Im\omega < 0$) do not coincide.
- The number of unstable eigenvalues is given by

$$n = \frac{1}{2\pi} \Delta\psi_C, \quad (91)$$

where $\Delta\psi_C$ is the increment of the argument of E along the contour in Fig. 25 (see e.g. [35] for a general description of the principle of the argument), which, due to the first symmetry in (90), can be written as twice the increment of the argument along the right half of the contour.

- $\omega = 0$ is an eigenvalue with geometric multiplicity 2 and associated eigenfunctions

$$\begin{aligned}(X^\pm, Y^\pm) &= (B_{GS\xi}^\pm, \bar{B}_{GS\xi}^\pm), \\ (X^\pm, Y^\pm) &= (iB_{GS}^\pm, -i\bar{B}_{GS}^\pm),\end{aligned}$$

which result from the two continuous symmetries of the system (63)-(64)

$$\xi \rightarrow \xi + c_1 \quad \text{and} \quad B^\pm \rightarrow e^{ic_2} B^\pm. \quad (92)$$

But its algebraic multiplicity is four because we have also two generalized eigenfunctions

$$\begin{aligned}(X^\pm, Y^\pm) &= (-i\partial B_{GS}^\pm/\partial c, i\partial \bar{B}_{GS}^\pm/\partial c), \\ (X^\pm, Y^\pm) &= (-i\partial B_{GS}^\pm/\partial \gamma, i\partial \bar{B}_{GS}^\pm/\partial \gamma),\end{aligned}$$

which come from the fact that $b^\pm = \partial B_{GS}^\pm/\partial c$ and $\bar{b}^\pm = \partial \bar{B}_{GS}^\pm/\partial \gamma$ satisfy

$$\begin{aligned}-B_{GS\xi} - (c+1)b_\xi^+ &= i[(\gamma + \phi_1^+)b^+ + (1 + \phi_2)b^- + \phi_3^+\bar{b}^+ + \phi_4\bar{b}^-], \\ -B_{GS\xi} - (c-1)b_\xi^- &= i[(\gamma + \phi_1^-)b^- + (1 + \bar{\phi}_2)b^+ + \phi_3^-\bar{b}^- + \phi_4\bar{b}^+],\end{aligned}$$

and

$$\begin{aligned}-iB_{GS} - (c+1)b_\xi^+ &= i[(\gamma + \phi_1^+)b^+ + (1 + \phi_2)b^- + \phi_3^+\bar{b}^+ + \phi_4\bar{b}^-], \\ -iB_{GS} - (c-1)b_\xi^- &= i[(\gamma + \phi_1^-)b^- + (1 + \bar{\phi}_2)b^+ + \phi_3^-\bar{b}^- + \phi_4\bar{b}^+],\end{aligned}$$

respectively, as it can be seen upon differentiation with respect to the soliton parameters c and γ in the GS equation, i.e., in the steady state version of (63)-(64) with $\varepsilon = 0$. In other words, the algebraic multiplicity is equal to four due to the four-dimensionality of the family of gap solitons (that can be parametrized in terms of c , γ and the two parameters in the continuous symmetries (92)),

but c and γ do not produce any increment of the geometric multiplicity because of the time-dependent character of change of variables performed in (63)-(64). The contribution to (91) of the fourth order root $\omega = 0$ is thus equal to -2 , see Fig. 25.

- The evaluation of the contribution of the outer arc in Fig. 25 requires to know the asymptotic behavior of E as $|\omega| \rightarrow \infty$. In this limit, eqs. (73)-(76) simplify drastically and the allowed solutions according to (88)-(89) are given, at first order, by

$$\begin{aligned} &(-e^{i\omega\xi/(1+c)}, 0, 0, 0), \quad (0, 0, -e^{i\omega\xi/(1+c)}, 0) \quad \text{for } \xi \geq 0 \quad \text{and} \\ &(0, \frac{-2\omega}{(1-c)}e^{-i\omega\xi/(1-c)}, 0, 0), \quad (0, 0, 0, \frac{2\omega}{(1-c)}e^{-i\omega\xi/(1-c)}) \quad \text{for } \xi \leq 0, \end{aligned}$$

recall that $\Im\omega > 0$. Therefore, $E(\omega) \sim \omega^2$ as $|\omega| \rightarrow \infty$, and the arc gives a contribution of amount 1 to (91).

- The second symmetry in (90) ensures that the Evans function is real in the segment of the real line that is not part of the essential spectrum (labeled 0 in Fig. 25) and its contribution to (91) is equal to $-n_o/2$, where n_o is the number of roots along the segment.
- The extended Evans function is not analytic at the edges of the essential spectrum but typically they do not contribute to (91) because $E \neq 0$ at $\omega = \pm\omega_{0,1}$ in a generic situation. The same argument can be used to conclude that, generically, there are no zeros in the rest of the essential spectrum (segments 1 and 2 in Fig. 25).

Collecting all the above mentioned contributions, the number of unstable eigenvalues can be finally written as

$$n = -n_0 - 1 + \frac{1}{\pi}(\Delta\psi_1 + \Delta\psi_2), \quad (93)$$

where $\Delta\psi_{1,2}$ represent the increment of the argument along the segments 1 and 2 in Fig. 25. Note that the formula above requires the evaluation of the Evans function only along the positive real axis.

The stability of the GS has been numerically analyzed using (93) for different values of the parameters c and γ . The evaluations of the Evans function have been

performed with an adaptive Runge-Kutta method of 4th order and the integrations have been started at $\xi = \pm\xi_\infty$, where ξ_∞ has been taken large enough to ensure that the GS amplitude is negligible at this point.

The results we have found are represented in Fig. 26 and can be summarized as follows: (i) the GS are unstable for values of γ smaller than a certain γ_c that is negative very small (see Fig. 26), and (ii) the onset of the instability always takes place through the collision of two real eigenvalues in the 0 segment in Fig. 25 that become complex with a nonzero value of $\Re\omega$ (temporal frequency) that is also presented in Fig. 26. For $\gamma < \gamma_c$ more eigenvalues become unstable, both with zero and nonzero temporal frequencies, but the stability is never regained.

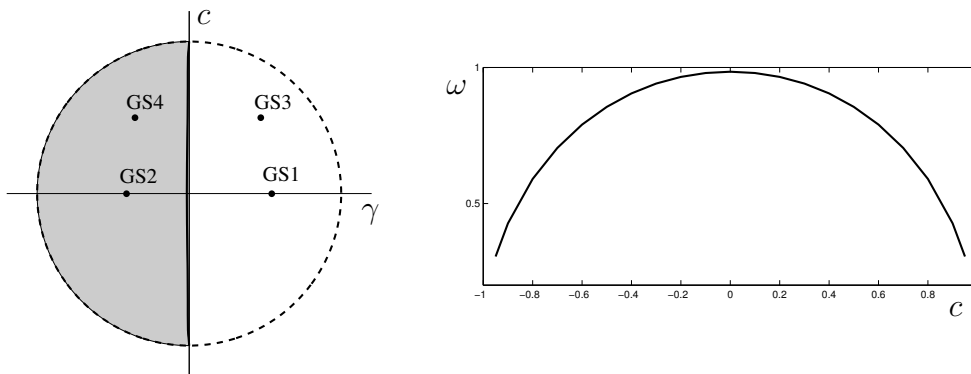


Figure 26: Left: GS stability diagram (shading indicates instability and dots correspond to the numerical simulations in Section 7.3). Right: frequency of the neutral mode at instability onset.

These stability results agree with those presented by Barashenkov and collaborators in [13, 14], which were calculated using Newton's method combined with a finite difference approximation on a finite interval of eqs. (73)-(76).

7.2 Perturbations with dispersive scales

We now complete the stability analysis of the GS with the study of the effect of perturbations that contain small dispersive scales, that is, scales with a typical size that goes as $\sqrt{|\varepsilon|}$ when $\varepsilon \rightarrow 0$.

In this case, the dispersion terms cannot be neglected in eqs. (65)-(66) and the eigenvalue problem that is obtained, after assuming exponential time dependence

(see eq. (72)), can be written as

$$\omega X^+ + i(c+1)X_\xi^+ = \varepsilon\kappa X_{\xi\xi}^+ + (\gamma + \phi_1^+)X^{++} + (1 + \phi_2)X^- + \phi_3^+ Y^+ + \phi_4 Y^-, \quad (94)$$

$$\omega X^- + i(c-1)X_\xi^- = \varepsilon\kappa X_{\xi\xi}^- + (\gamma + \phi_1^-)X^{--} + (1 + \bar{\phi}_2)X^+ + \phi_3^- Y^- + \phi_4 Y^+, \quad (95)$$

$$-\omega Y^+ - i(c+1)Y_\xi^+ = \varepsilon\kappa Y_{\xi\xi}^+ + (\gamma + \phi_1^+)Y^{++} + (1 + \bar{\phi}_2)Y^- + \bar{\phi}_3^+ X^+ + \bar{\phi}_4 X^-, \quad (96)$$

$$-\omega Y^- - i(c-1)Y_\xi^- = \varepsilon\kappa Y_{\xi\xi}^- + (\gamma + \phi_1^-)Y^{--} + (1 + \phi_2)Y^+ + \bar{\phi}_3^- X^- + \bar{\phi}_4 X^+, \quad (97)$$

where the eigenfunctions (X^\pm, Y^\pm) must decay to zero as $\xi \rightarrow \pm\infty$.

If we now introduce the fast (dispersive) spatial variable $\eta = \xi/\sqrt{|\varepsilon|}$ and expand the solution of the system above as

$$\begin{aligned} (X^\pm, Y^\pm) &= (X_0^\pm, Y_0^\pm)(\eta, \xi) + \sqrt{|\varepsilon|}(X_1^\pm, Y_1^\pm)(\eta, \xi) + \dots, \\ \omega &= \omega_0/\sqrt{|\varepsilon|} + \omega_1 + \dots, \end{aligned}$$

with $|\varepsilon| \ll 1$, we obtain, at leading order, the following uncoupled homogeneous system

$$\omega_0 X_0^+ + i(c+1)X_{0\eta}^+ = 0, \quad (98)$$

$$\omega_0 X_0^- + i(c-1)X_{0\eta}^- = 0, \quad (99)$$

$$-\omega_0 Y_0^+ - i(c+1)Y_{0\eta}^+ = 0 \quad (100)$$

$$-\omega_0 Y_0^- - i(c-1)Y_{0\eta}^- = 0, \quad (101)$$

whose solutions are of the form

$$X_0^\pm = A_0^\pm(\xi)e^{i\omega_0\eta/(c\pm 1)},$$

$$Y_0^\pm = B_0^\pm(\xi)e^{i\omega_0\eta/(c\pm 1)},$$

where ω_0 has to be purely real for the eigenfunctions to be bounded in the short scale η . These expressions represent travelling waves that propagate in η to the left (+) and right (-), with velocities $1+c$ and $1-c$, respectively, and exhibit modulations in the longer scale $\xi \sim 1$.

At next order, a system is obtained for (X_1^\pm, Y_1^\pm) that is identical to (98)-(101) but with a nonzero right hand side. The equations for $(A_0^\pm(\xi), B_0^\pm(\xi))$ result from applying solvability conditions to this system, i.e., from forcing (X_1^\pm, Y_1^\pm) to remain

bounded in the fast scale, and are given by

$$\omega_1 A_0^+ + i(c+1)A_{0\xi}^+ = (\gamma + \phi_1^+ - \frac{\varepsilon}{|\varepsilon|} \kappa \frac{\omega_o^2}{(c+1)^2}) A_0^+ + \phi_3^+ B_0^+, \quad (102)$$

$$\omega_1 A_0^- + i(c-1)A_{0\xi}^- = (\gamma + \phi_1^- - \frac{\varepsilon}{|\varepsilon|} \kappa \frac{\omega_o^2}{(c-1)^2}) A_0^- + \phi_3^- B_0^-, \quad (103)$$

$$-\omega_1 B_0^+ - i(c+1)B_{0\xi}^+ = (\gamma + \phi_1^+ - \frac{\varepsilon}{|\varepsilon|} \kappa \frac{\omega_o^2}{(c+1)^2}) B_0^+ + \bar{\phi}_3^+ A_0^+, \quad (104)$$

$$-\omega_1 B_0^- - i(c-1)B_{0\xi}^- = (\gamma + \phi_1^- - \frac{\varepsilon}{|\varepsilon|} \kappa \frac{\omega_o^2}{(c-1)^2}) B_0^- + \bar{\phi}_3^- A_0^-, \quad (105)$$

together with the conditions that $A_0^\pm \rightarrow 0$ and $B_0^\pm \rightarrow 0$ as $\xi \rightarrow \pm\infty$.

Notice that, as it happened for the CW in Section 5.2, dispersive perturbations propagating to the left (+) and right (-) are uncoupled and the system above is composed of two second order independent subsystems: (102),(104) and (103),(105).

In the limit $\xi \rightarrow \pm\infty$, we have $\phi_1^\pm \rightarrow 0$ and $\phi_3^\pm \rightarrow 0$ (see (67) and (69)) and the first subsystem becomes a constant coefficient, diagonal system with associated spatial exponents λ ,

$$(A_0^+, B_0^+) = (\alpha, \beta) e^{i\lambda\xi},$$

of the form

$$\lambda = (\omega_1 \pm (\gamma - \frac{\varepsilon}{|\varepsilon|} \kappa \frac{\omega_o^2}{(c+1)^2})) / (c+1).$$

Both spatial exponents have the same imaginary part and for $\Im\omega_1 \neq 0$ the two corresponding asymptotic behaviors grow simultaneously unbounded as either $\xi \rightarrow +\infty$ or $\xi \rightarrow -\infty$ (depending on the sign of $\Im\omega_1$), and therefore there is no other possible bounded solution apart from the zero solution. The same holds true for the second subsystem and allows us to conclude that there are no instabilities associated with the perturbations with small dispersive scales.

In contrast to what was obtained for the CW in Section 5.2, the GS do not exhibit dispersive instabilities. The required spatial decay of the dispersive perturbations as $\xi \rightarrow \pm\infty$ can only be achieved through the coupling that comes from the nonlinear interaction terms in the NLCME (see eqs. (102)-(105)), which remains nonzero for the CW but vanishes in the GS case as $\xi \rightarrow \pm\infty$.

7.3 Numerical simulations of the amplitude equations

The GS stability predictions are cross-checked here against the results of the numerical simulation of the NLCME with small dispersion terms (33)-(35).

The code developed for the numerical integration of equations (33)-(35) assumes periodic boundary conditions (see Appendix A). In order to simulate the NLCME in an infinite domain we take a spatial period large as compared with the characteristic length of the GS (L_∞) and we then rescale space, time and the size of amplitudes to make the spatial period one and the group velocity and the first nonlinear coefficient also equal to one (see Fig. 27 for the explicit expressions of the rescalings). Note that after these changes of variables the resulting strength of the grating, κ , is increased and the dispersion, ε , is reduced. Note also that the validity of the numerical simulations is limited in time because the finite length effects will eventually contaminate the solution on the whole domain.

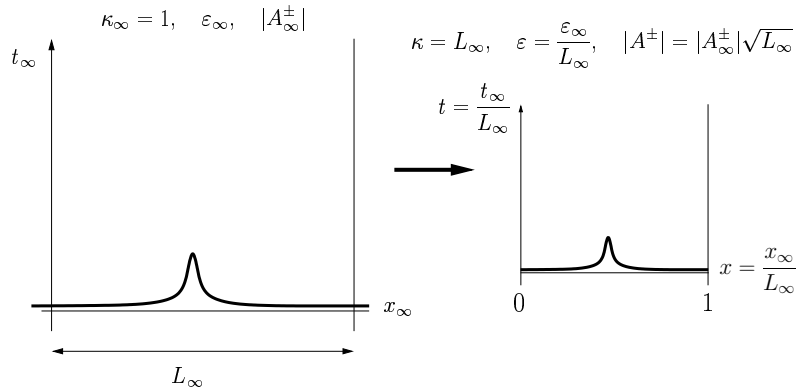


Figure 27: Rescalings performed to transform the large finite domain of size L_∞ into $[0, 1]$.

We present the results of four simulations with parameters $\sigma = \frac{1}{2}$, $\kappa = 40$ and $\varepsilon = 0$ (dispersion is not considered in this first set of simulations because we are interested only in instabilities due to perturbations without dispersive scales) starting from the following GS with a small random perturbation of size $\sim 10^{-3}$ superimposed:

- GS1: $c = 0$ and $\gamma = \cos 1 = .5403 \dots$
- GS2: $c = 0$ and $\gamma = \cos 2 = -.4165 \dots$
- GS3: $c = 0.5$ and $\gamma = \frac{\sqrt{3}}{2} \cos 1 = .4679 \dots$

- GS4: $c = 0.5$ and $\gamma = \frac{\sqrt{3}}{2} \cos 2 = -.3604\dots$

According to the stability analysis of the previous section, the GS1 is a stable soliton ($\gamma > 0$ in Fig. 26). The simulation results are consistent with this: the norm of the solution and its derivatives is almost constant for 50 time units with only a small variation due to the initial perturbation (see top plot in Fig. 28), and the $x - t$ diagram in Fig. 28 indicates that the spatial profiles of the modulus of the amplitudes remain practically unaltered, as it should be for a GS with zero propagation velocity.

On the other hand, the GS2 is unstable (see Fig. 26) and the rapid development of the oscillatory instability can be clearly appreciated from the simulation results plotted in Fig. 29. From the evolution of the norm of the solution in the top plot of Fig. 29 the frequency of the most unstable mode can be estimated $\omega_{\text{estimated}} \simeq 1.34\dots$, and this number is in very good agreement with the real part of the unstable eigenvalue, $\omega \simeq 1.33\dots + i0.0338\dots$, computed applying Newton's method to find the zero of the Evans function. This is actually the only unstable eigenvalue as it can be seen in the map of the zeros of the Evans function that is also included in the middle plot of Fig. 29.

The GS3 is a stable soliton (see Fig. 26) that now propagates with velocity 0.5, and the results of the simulation presented in Fig. 30 corroborate again the conclusions of the stability analysis: the norms remain almost constant and the $x - t$ diagram shows the soliton propagating to the right without any perceptible distortion after 50 units of time (note that now the amplitudes of the GS are not equal because this is a travelling pulse, $y \neq 0$ in (56)-(58)).

And for the last case, the GS4, the stability results indicate that it corresponds to an unstable propagative soliton (see Fig. 26) and this is in good agreement with the simulation results presented in Fig. 31. The instability that develops is again oscillatory and its frequency estimated from the norm evolution of the solution, $\omega_{\text{estimated}} \simeq 1.17\dots$, is again very close to the unstable eigenvalue obtained solving the equation $E(\omega) = 0$, $\omega \simeq 1.166\dots + i0.0218\dots$ (middle plot of Fig. 31). Also, the growth rate computed from $E(\omega) = 0$ is now smaller than in the GS2 case and produces a slower instability development, as it can be appreciated from the time plots of $\|A_x^\pm\|$ in Figs. 29 and 31.

Finally, in order to complete the numerical checking of the stability results, we

have performed several simulations of the stable solitons GS1 and GS3 with $\kappa = 40$ and different values of the dispersion coefficient, namely, $\varepsilon = \pm 4 \cdot 10^{-4}$, $\pm 2 \cdot 10^{-4}$ and $\pm 10^{-4}$. The numerics corroborate the theoretical results obtained in Section 7.2, that is, no sign of any dispersive instabilities was detected. The numerical solutions found were indistinguishable from those represented in Figs. 28 and 30 and therefore their plots are omitted.

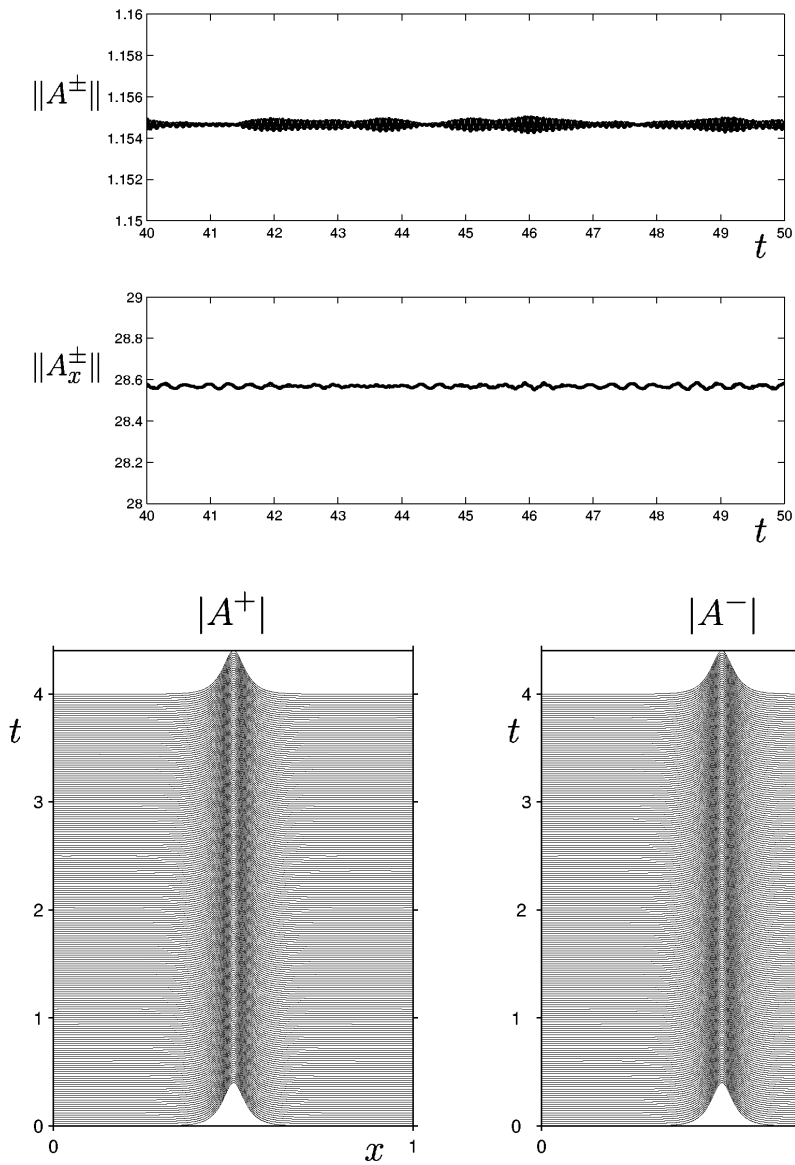


Figure 28: Top: thick (thin) lines indicate the time evolution of the spatial norm of A^+ (A^-) and its spatial derivative, for $\sigma = \frac{1}{2}$, $\kappa = 40$ and $\varepsilon = 0$. The initial condition is the GS1 with a random perturbation of size $\sim 10^{-3}$. Bottom: space-time representation of the solution for four time units right after $t = 50$ in the top plot.

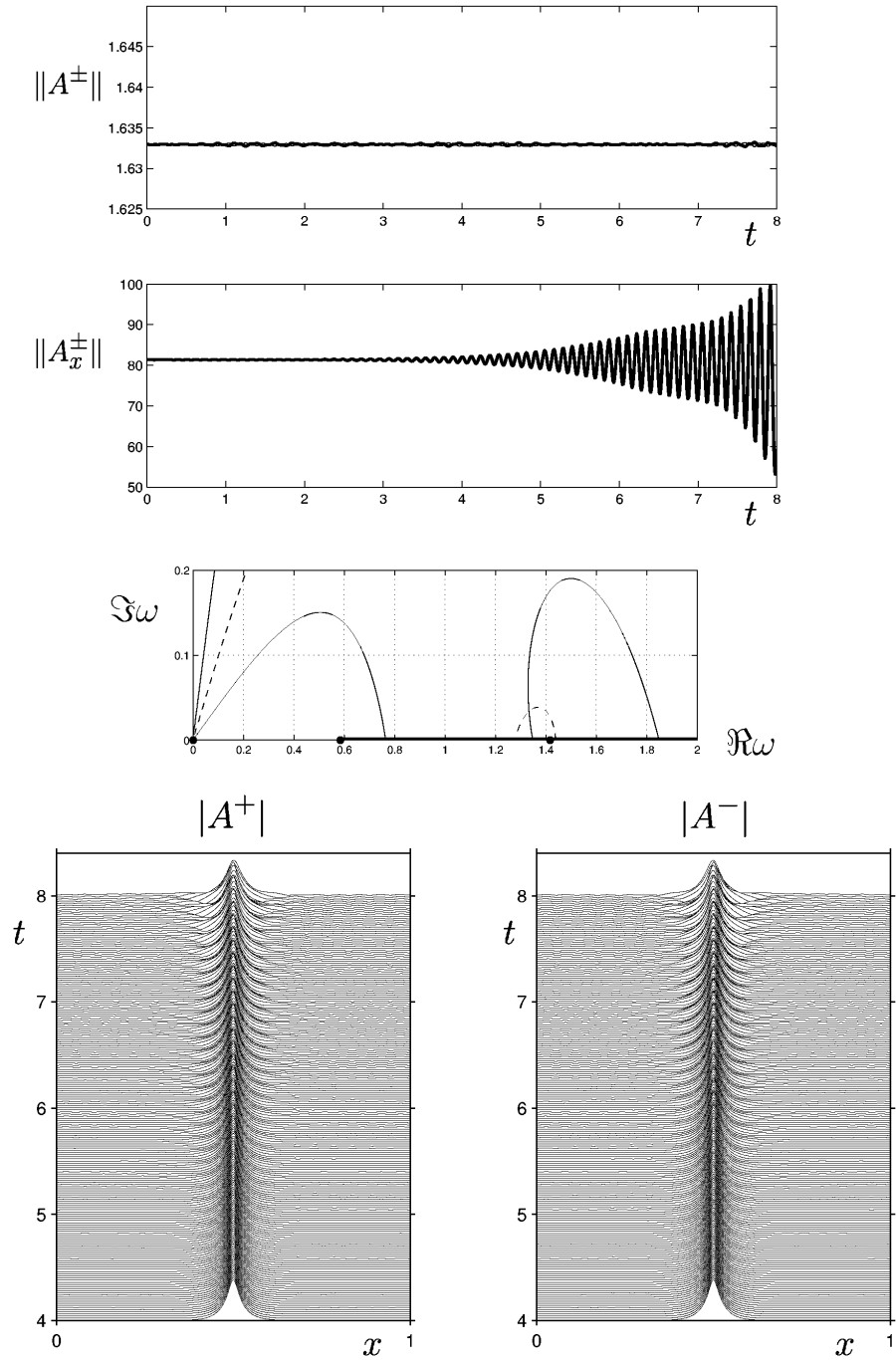


Figure 29: Top: thick (thin) lines indicate the time evolution of the spatial norm of A^+ (A^-) and its spatial derivative, for $\sigma = \frac{1}{2}$, $\kappa = 40$ and $\varepsilon = 0$. The initial condition is the GS2 with random perturbation of size $\sim 10^{-3}$. Middle: $\Re E(\omega) = 0$ ($\Im E(\omega) = 0$) contours in the complex ω plane in solid (dashed) line. Bottom: space-time representation of the solution for the last four time units in the top plot.

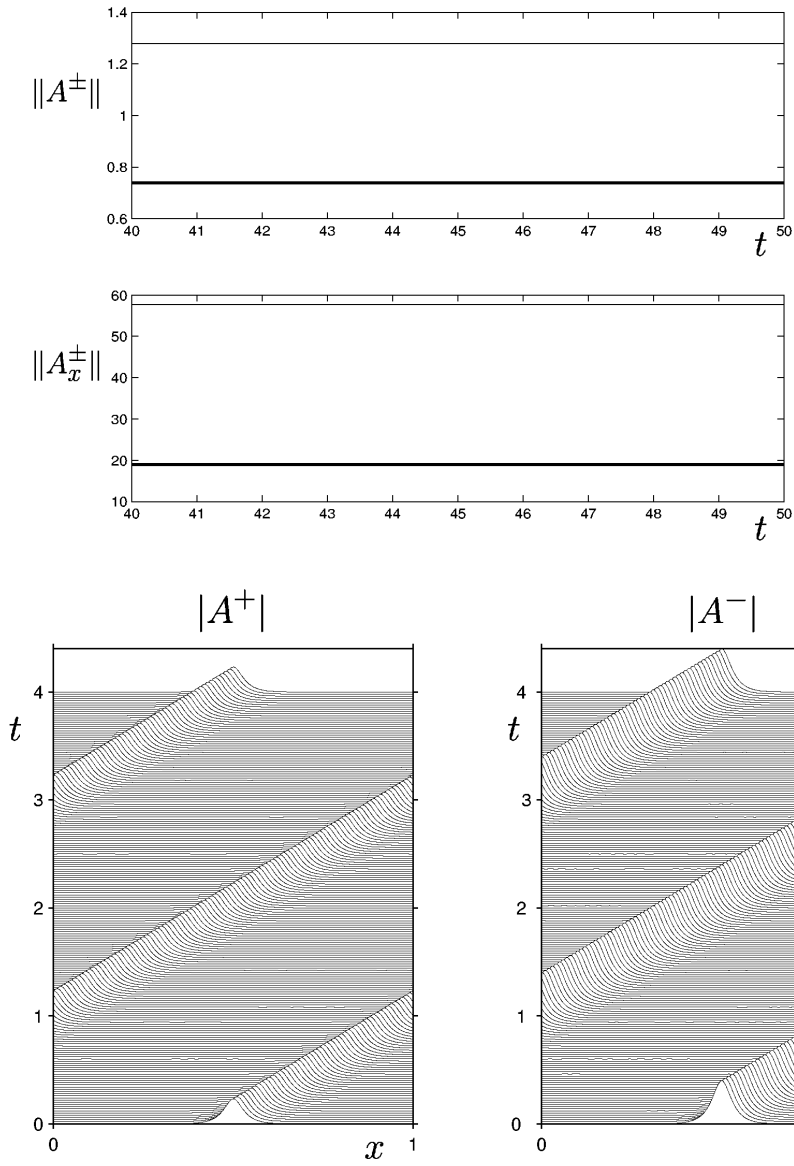


Figure 30: Top: thick (thin) lines indicate the time evolution of the spatial norm of A^+ (A^-) and its spatial derivative, for $\sigma = \frac{1}{2}$, $\kappa = 40$ and $\varepsilon = 0$. The initial condition is the GS3 with random perturbation of size $\sim 10^{-3}$. Bottom: space-time representation of the solution for four time units right after $t=50$ in the top plot.

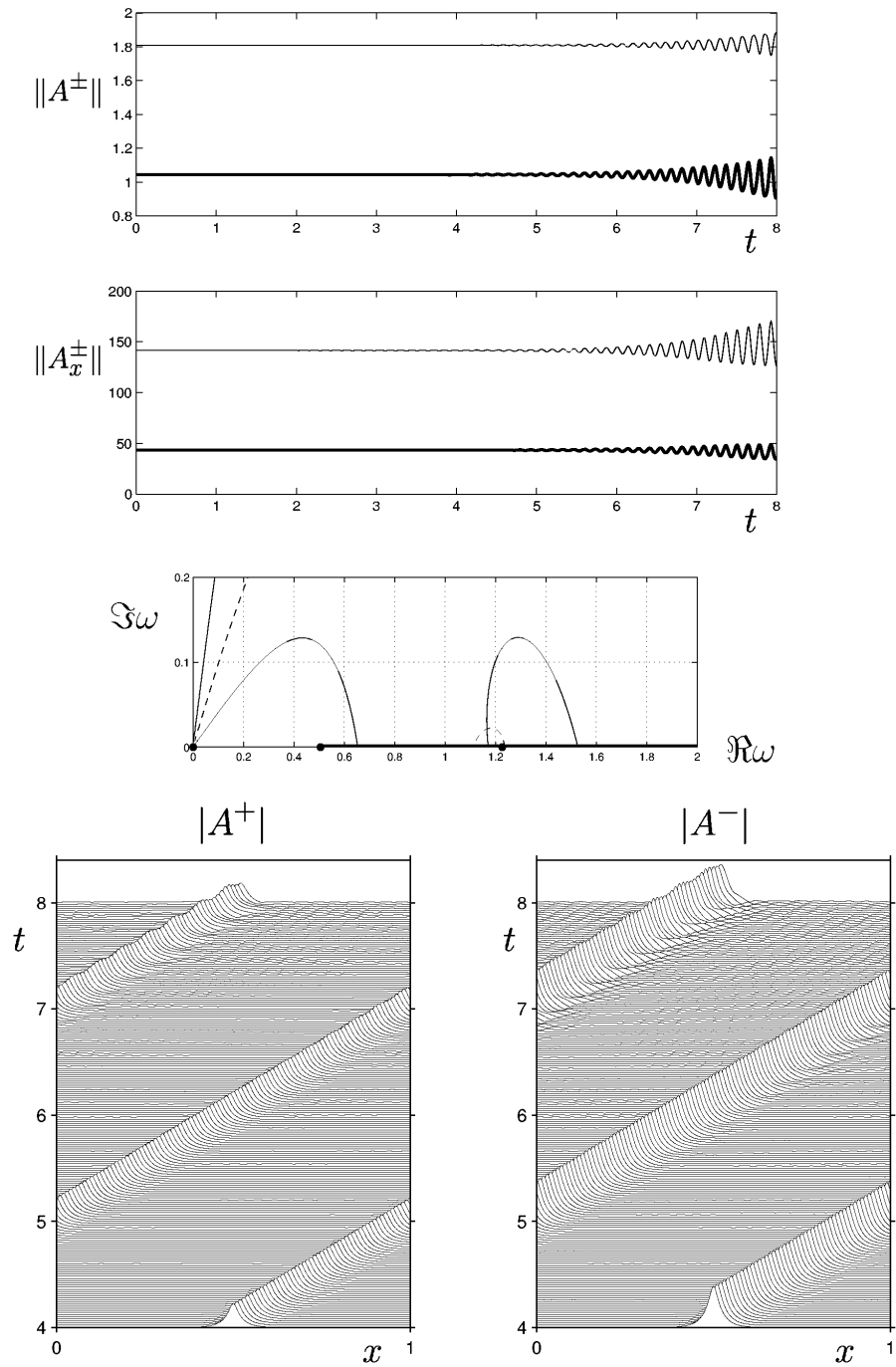


Figure 31: Top: thick (thin) lines indicate the time evolution of the spatial norm of A^+ (A^-) and its spatial derivative, for $\sigma = \frac{1}{2}$, $\kappa = 40$ and $\varepsilon = 0$. The initial condition is a GS4 with random perturbation of size $\sim 10^{-3}$. Middle: $\Re E(\omega) = 0$ ($\Im E(\omega) = 0$) contours in the complex ω plane in solid (dashed) line. Bottom: space-time representation of the solution for the last four time units in the top plot.

8 Numerical simulations of the MLE

In order to confirm the validity of the amplitude equations with small dispersion terms and the theoretical stability results obtained in the previous sections, we have tested them against numerical simulations of the complete MLE (16)-(17).

The MLE simulations correspond to a ring shaped fiber grating geometry with a large number of refractive index oscillations, that is, to periodic boundary conditions,

$$E(x + L, t) = E(x, t), \quad P(x + L, t) = P(x, t),$$

with $L \gg 1$, see Appendix B for the details of the numerical method. The initial conditions used in all the simulations are slightly perturbed CW and GS configurations.

The relation between the solutions of the MLE (16)-(17) and the amplitude equations (33)-(35), after taking into account the rescalings in (32), can be written as

$$\begin{Bmatrix} E \\ P \end{Bmatrix} = \begin{Bmatrix} \omega^2 \\ 1 - \omega^2 \end{Bmatrix} \sqrt{\frac{v_g}{L|u_2|}} (\bar{A}^+ e^{ix+i\omega t} + \bar{A}^- e^{-ix+i\omega t}) + \text{c.c.} + \dots \quad (106)$$

The grating strength and the dispersion are related to their scaled counterparts by

$$\Delta n = \frac{v_g}{L|w|} \kappa \quad \text{and} \quad \varepsilon = -\frac{d}{Lv_g}, \quad (107)$$

where $L \gg 1$ and the parameters ω , v_g , d , w and u_2 are given by (15), (24), (25), (26) and (27) as functions of ω_p^2 and n_0^2 only.

The structure of the actual physical patterns that result from (106) becomes more clear if we rewrite the electric field as

$$E \sim (\bar{A}^+ e^{i\omega t} + A^- e^{-i\omega t}) e^{ix} + \text{c.c.} + \dots,$$

where the amplitudes A^\pm depend slowly on space and time and thus remain approximately constant in any region of extent $\Delta x \sim 1$ and for any time interval $\Delta t \sim 1$. The complex number inside parentheses in the expression above,

$$\bar{A}^+ e^{i\omega t} + A^- e^{-i\omega t} = M e^{i\varphi},$$

can be regarded as the sum of two constant complex numbers that rotate with opposite angular velocity ω (Fig 32a) and its modulus, M , gives the local amplitude of the envelope of the pattern,

$$E \sim M e^{i\varphi + ix} + \text{c.c.} + \dots \sim M \cos(x + \varphi) + \dots,$$

see Fig 32b, that oscillates in time between the extreme values

$$M_{\max} = ||A^+| + |A^-|| \quad \text{and} \quad M_{\min} = ||A^+| - |A^-||.$$

Therefore, if the amplitudes are nearly equal in a certain region, $|A^+| \simeq |A^-|$, then M will oscillate between 0 and M_{\max} and φ will alternate between $\pm(\varphi_{A^+} + \varphi_{A^-})/2$ (see Fig32a), and the pattern will locally look like a SW. On the other hand, if one of the amplitudes dominates, $|A^+| \gg |A^-|$, then M is almost constant and φ behaves approximately like ωt , and the pattern resembles a TW. For any other configuration with arbitrary A^+ and A^- the resulting pattern will look more complicated; it will be a superposition of SW and TW.

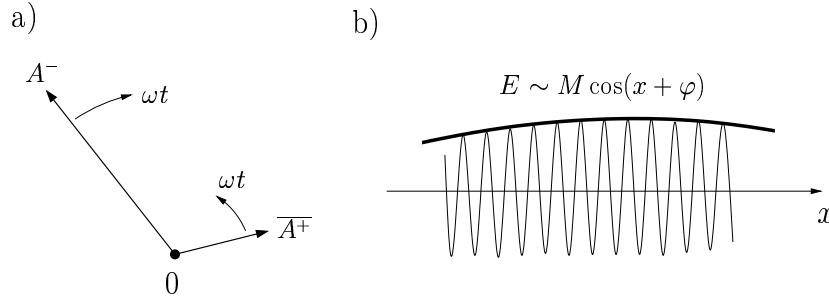


Figure 32: Construction of the solution of the MLE from the amplitudes A^\pm .

All CW simulations (shown in Figs. 33 to 37) have been carried out using the following parameters: $\omega_p^2 = 1$, $n_0^2 = 2$ and $L = 64(2\pi)$ (i.e., there are 128 oscillations of the grating inside the fiber ring). For every simulation, the corresponding value of Δn is calculated from κ using eq. (107) and the sign of the dispersion is selected by either choosing the + or the - sign in the equation for ω (15), see Fig. 3. The number of Fourier modes and the time step used in the numerical scheme are $M_{\text{Fourier}} = 512$ and $\Delta t = .01$ (see Appendix B).

In the results presented in Fig. 33 the initial condition is given by the CW1 in Fig. 12 with a small perturbation superimposed. The first and second plot show the time evolution of the norm of the electric field,

$$\|E\| = \sqrt{\frac{1}{L} \int_0^L |E|^2 dx},$$

and correspond, respectively, to $\omega = \omega^-$ and $\omega = \omega^+$, that is, to negative and positive dispersion (see eq (107) and Fig. 3). The electric field pattern for the CW1 is a uniform SW. The associated value of $\|E\|$ oscillates very fast in time between 0 and its maximum value, but this oscillation is too fast to be appreciated in the first two plots of Fig. 33 and they just look like black patches. The MLE simulations confirm the theoretical predictions: the CW1 is stable for negative dispersion (first plot in Fig. 33) and unstable for positive dispersion (something starts to develop around $t = 60000$ in the second plot). The corresponding spatial profiles of E at $t = 75000$ are given in the third and fourth plots of Fig 33: for negative dispersion (third plot) a perfectly uniform oscillatory pattern is obtained but, for positive dispersion, a modulation is clearly present (fourth plot). In order to be sure that this is a dispersive instability we have repeated the unstable ($\omega = \omega^+$) MLE simulation in a four times longer domain ($L = 256(2\pi)$). The resulting spatial profile of E at $t = 160000$ is shown in the last plot of Fig. 33. Notice how the number of basic wavelengths is now four times higher but the number of wavelengths of the modulation only approximately doubles (increases from 5 to 9), indicating the onset of dispersive scales whose size goes as $\sqrt{L} \sim \frac{1}{\sqrt{\epsilon}}$.

Dispersion is negative in the simulation shown in Fig. 34, which starts from a small perturbation of the CW2 in Fig. 12. According to the stability results from Section 5, this CW is unstable and evolves to a spatially uniform, time periodic solution (see Fig. 16). The solution of the MLE reproduces this behavior: the fast oscillations of $\|E\|$ in the top plot slowly alternate between going down to zero (nearly equal amplitudes) and remaining away from zero (different amplitudes), and E does not develop any slow spatial modulation (see bottom plot of Fig. 34).

Fig. 35 corresponds to a MLE simulation starting from the CW3 in Fig. 17 and with negative dispersion. The linear theory now predicts a destabilization due to a mode with one single wavelength inside the ring. This is again corroborated by the

MLE simulation results, as it can be appreciated from the bottom plot of Fig. 35 that shows the spatial profile of E at the beginning of the instability development. For longer times, the $\|E\|$ plot in Fig. 35 indicates that the solution becomes more complicated.

The initial condition for the two MLE simulations in Fig. 36 is the CW defined by the parameters $\kappa = 1$, $\theta = \frac{\pi}{4}$ and $\rho^2 = 1$ (see Fig. 12) with a small perturbation. The first and third plot correspond to positive dispersion and indicate that the CW is stable. The dispersion is negative in the second and fourth plot where the destabilization of the CW can be clearly seen in the time evolution of $\|E\|$ and the spatial profile of E shows dispersive modulations. This is in perfect agreement again with the linear stability results in Section 5.

Fig. 37 shows the last of the CW related MLE simulations. Dispersion is taken positive in this case and the initial condition is a perturbed CW with parameters $\kappa = 2$, $\theta = \frac{\pi}{4}$ and $\rho^2 = 3$, which corresponds to a point in Fig. 17 above the point labeled 4 and inside the shaded unstable region. As the stability calculations predicted, the solution develops dispersive scales (see lower plot in Fig. 37) and the development of the instability is now faster than in the previous cases (top plot in Fig. 37) because now, as we saw in Section 5, the range of unstable wavenumbers is larger: it begins in the transport regime and extends up to the dispersive region.

The aim of the subsequent MLE simulations is to check the GS stability predictions obtained in Section 7. To this end, we use perturbed GS as initial conditions and we set $\kappa = 40$ and $L = 512(2\pi)$ to approximate an infinite geometry by means of a large ring. The rest of the parameters are left unchanged, $\omega_p^2 = 1$, $n_0^2 = 2$, and the number of Fourier modes and the time step used in the numerics are $M_{\text{Fourier}} = 4096$ and $\Delta t = .01$.

The first three plots in Fig. 38 corresponds to a MLE simulation that starts from GS1 in Fig. 26. According to the theoretical results from Section 7, this is a stable soliton and this is also what is obtained from the MLE simulation. The time evolution of $\|E\|$ (first plot in Fig. 38) exhibits a fast oscillation between 0 (the $c = 0$ GS have equal amplitudes) and its constant maximum value. And the snapshots of the spatial profiles of E at two different times (second and third plot) show that the GS remains practically unchanged.

The initial condition used in the last two plots in Fig. 38 is the GS2 in Fig.

26. This GS is unstable and this is what is found also in the simulation. The development of the instability produces a slow time modulation in the fast oscillation of $||E||$ (fourth plot) and the distortion of the GS can be seen in the snapshot of E (last plot).

The GS2 and GS4 in Fig. 26 are the initial conditions of the simulations presented in Fig. 39. The GS2 is a stable moving soliton and this is confirmed by the uniform oscillations of $||E||$ in the first plot of Fig. 39 and the snapshots of E (second and third plot) that show a translated undistorted GS. Notice that the GS amplitudes are not equal in this case and thus the minimum of fast oscillation of $||E||$ is not 0.

The GS4 is unstable and again this is reproduced in the MLE simulation: a slow time oscillation can be appreciated in the time evolution of $||E||$ (fourth plot) and the MLE solution moves away from the GS as time advances (see the spatial profile of E in the bottom plot of Fig. 39).

Finally, in agreement with the stability results presented in Section 7, the MLE simulations showed no sign of any dispersive instabilities associated with GS. The simulations in Figs. 38 and 39 correspond to negative dispersion ($\omega = \omega^-$), but the same simulations were run with positive dispersion ($\omega = \omega^+$) and no significant qualitative stability differences were found.

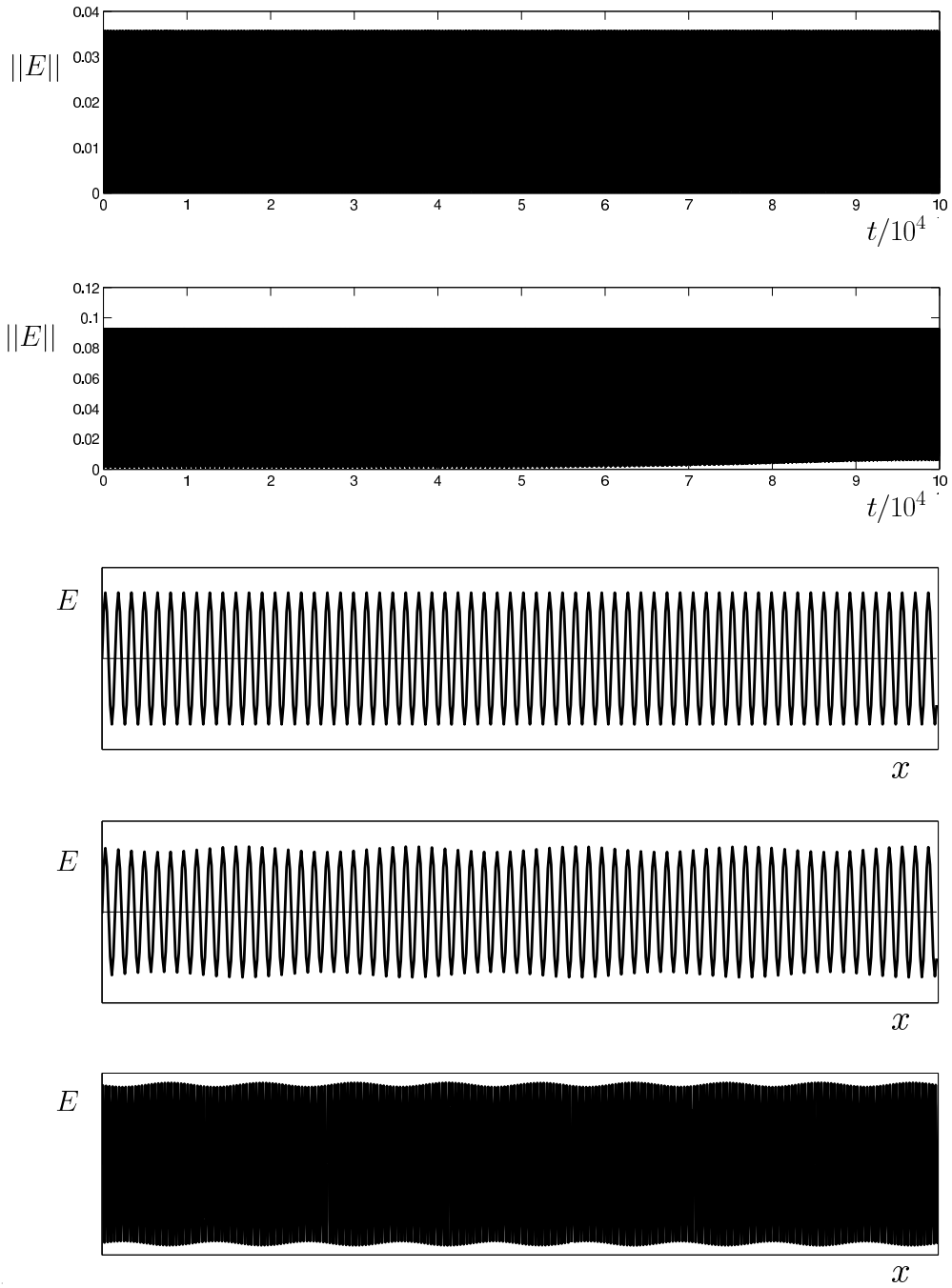


Figure 33: MLE simulation results starting from a CW ($\kappa = 1$, $\theta = -\frac{\pi}{4}$ and $\rho^2 = 1$) with a 10^{-4} perturbation. From top to bottom: time evolution of the norm of E for ω^- and ω^+ , spatial profiles of E at $t = 75000$ for ω^- and ω^+ , and spatial profile of E at $t = 160000$ for ω^+ and $L = 512\pi$.

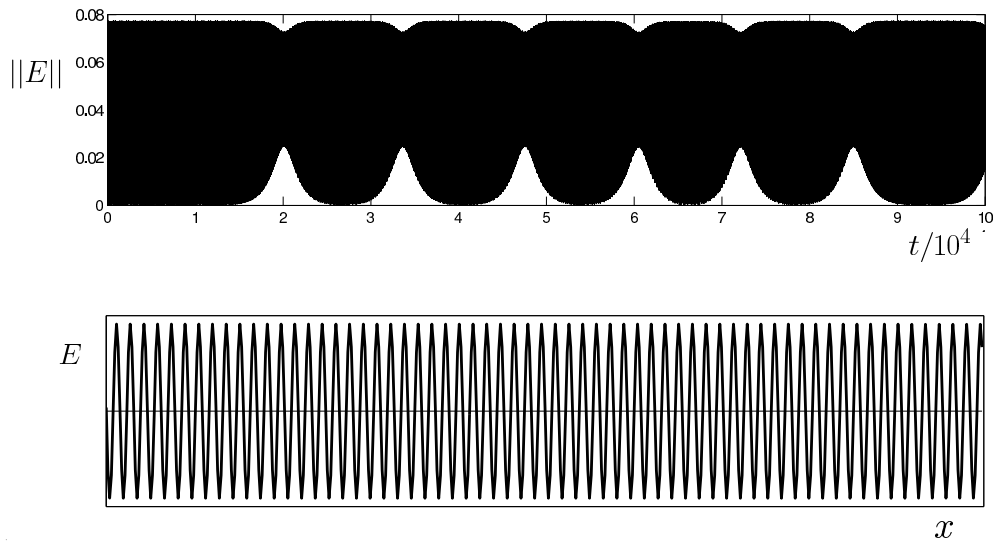


Figure 34: MLE simulation results starting from a CW ($\kappa = 1$, $\theta = -\frac{\pi}{4}$ and $\rho^2 = 4.5$) with a 10^{-4} perturbation. Time evolution of the norm of E for ω^- and spatial profile of E at $t = 88000$.

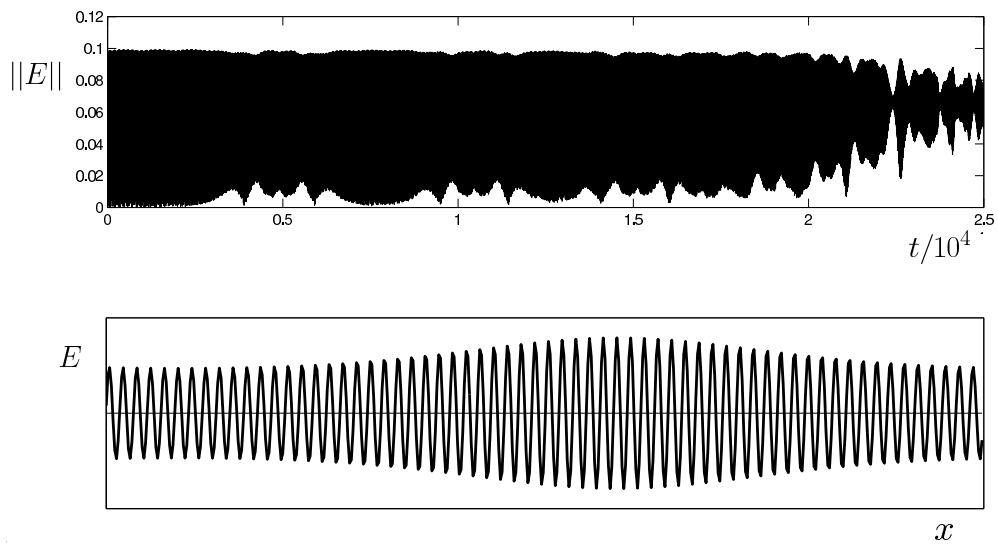


Figure 35: MLE simulation results starting from a CW ($\kappa = 2$, $\theta = -\frac{\pi}{4}$ and $\rho^2 = 7.2$) with a 10^{-4} perturbation. Time evolution of the norm of E for ω^- and spatial profile of E at $t = 4500$.

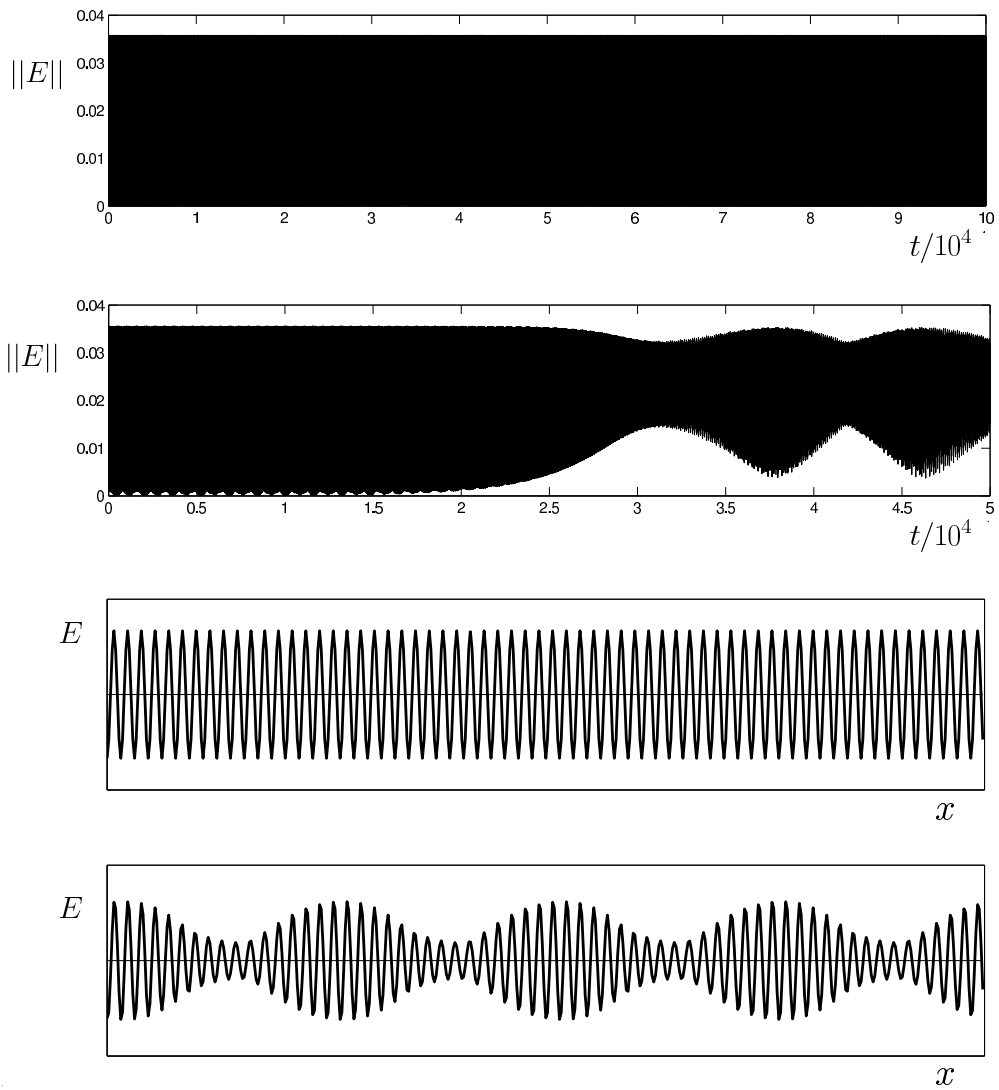


Figure 36: MLE simulation results starting from a CW ($\kappa = 1$, $\theta = \frac{\pi}{4}$ and $\rho^2 = 1$) with a 10^{-4} perturbation. From top to bottom: time evolution of the norm of E for ω^+ and ω^- , spatial profile of E at $t = 75000$ and ω^+ , and spatial profile of E at $t = 30000$ for ω^- .

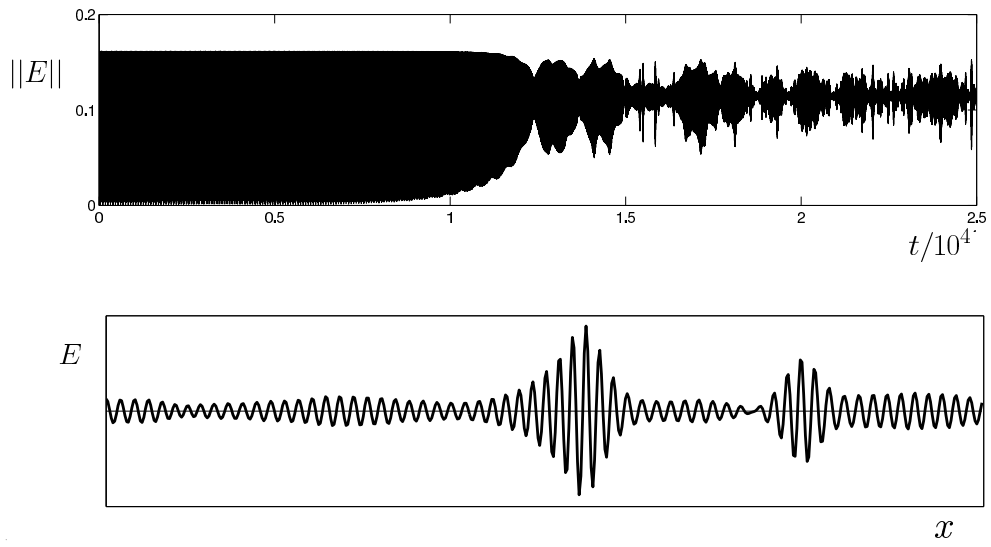


Figure 37: MLE simulation results starting from a CW ($\kappa = 2$, $\theta = \frac{\pi}{4}$ and $\rho^2 = 3$) with a 10^{-4} perturbation. Time evolution of the norm of E for ω^+ and spatial profile of E at $t = 18000$.

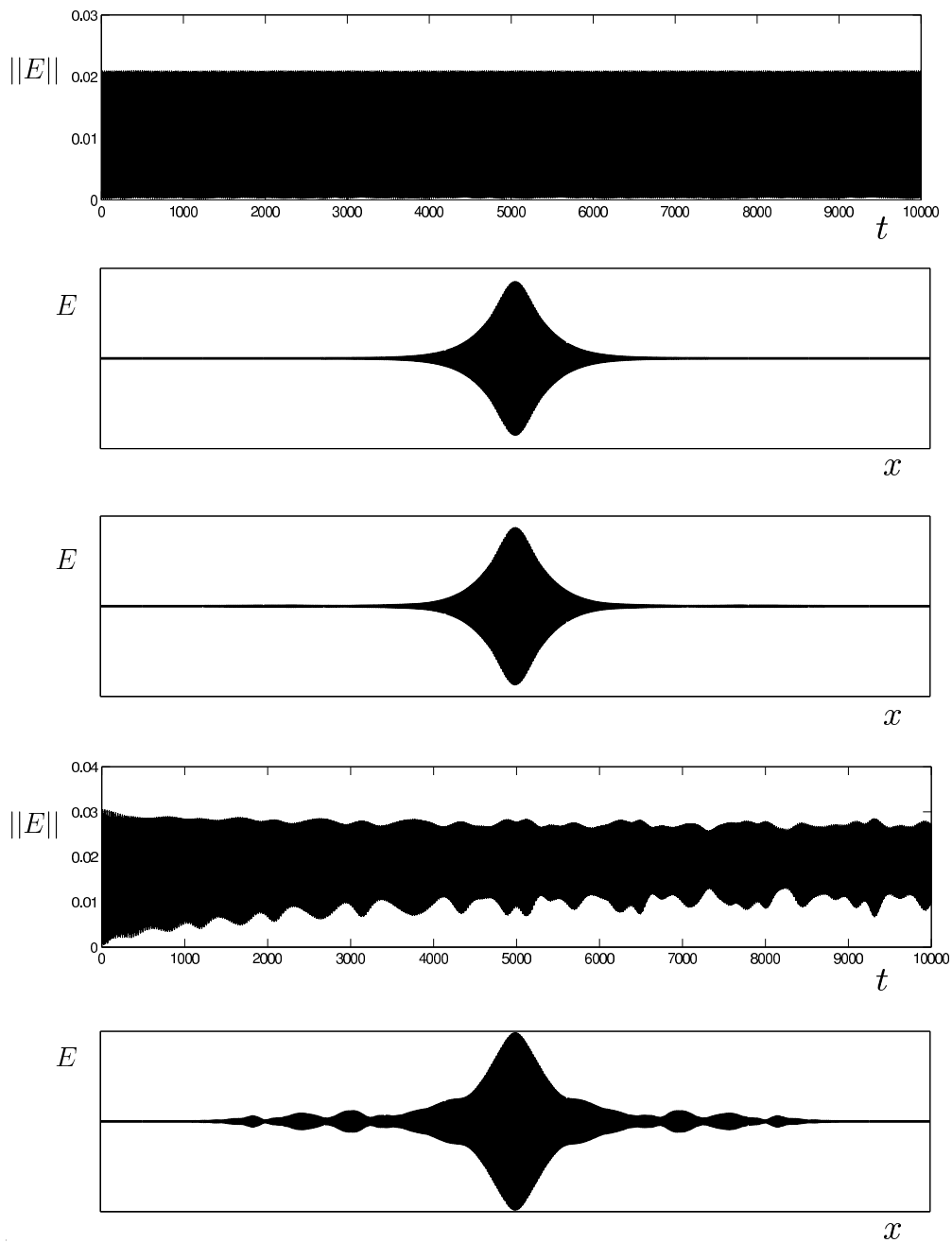


Figure 38: MLE simulation results for ω^- and starting from a GS with a 10^{-4} perturbation. From top to bottom: time evolution of the norm of E starting from GS1 ($c = 0$ and $\gamma = \cos 1$), spatial profiles of E at $t = 200$ and 9000 , time evolution of the norm of E starting from GS2 ($c = 0$ and $\gamma = \cos 2$) and spatial profile of E at $t = 2500$.

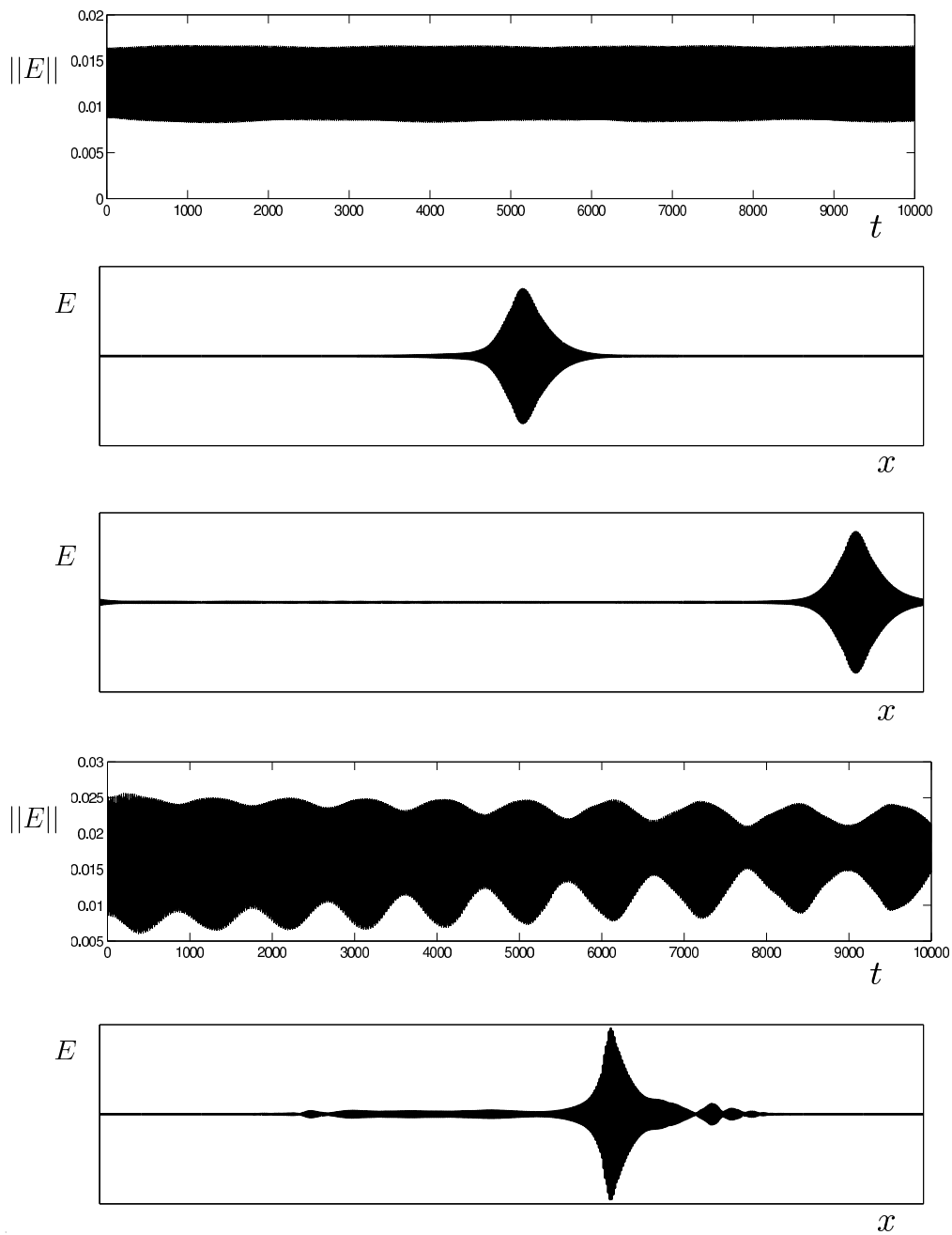


Figure 39: MLE simulation results for ω^- and starting from a GS with a 10^{-4} perturbation. From top to bottom: time evolution of the norm of E starting from GS3 ($c = 0.5$ and $\gamma = \frac{\sqrt{3}}{2} \cos 1$), spatial profiles of E at $t = 150$ and 6500 , time evolution of the norm of E starting from GS4 ($c = 0$ and $\gamma = \frac{\sqrt{3}}{2} \cos 2$) and spatial profile of E at $t = 2000$.

9 Concluding remarks

Material dispersion terms are systematically neglected in the standard amplitude equation formulation (NLCME) used in the literature to describe the weakly non-linear dynamics of light propagation in fiber gratings. We have analyzed in this report the effect of dispersion in the light propagation patterns that set in the fiber grating. To be more precise, this work focuses on the effect of dispersion on the stability of two important families of solutions, namely, the continuous waves (CW) and the gap solitons (GS). We have obtained precise theoretical linear stability results that have been successfully cross-checked against exhaustive numerical simulations of the amplitude equations with small dispersion terms (33)-(35) and of the complete physical model equations for light propagation in a fiber grating, i.e., the MLE (16)-(17). The development of the numerical codes required to carry out the two sets of simulations described above has also been part of the present research effort.

The main results in this report can be summarized as follows:

- The stability of the CW is drastically affected by dispersion. No matter how small is the dispersion or what sign it has, there are always stable CW according to the NLCME formulation that are dispersively unstable. The destabilization produced by the small dispersive terms is not a higher order, longer time effect; it takes place in the time scale of the NLCME and the associated growth rates remain of order one as the dispersion coefficient goes to zero.
- The dispersion induced instability generates dispersive scales that are small ($\sim \sqrt{L} \gg 1$) as compared with typical scale of the NLCME ($\sim L \gg 1$) but still large as compared with the wavelength of the basic wavetrains (~ 1). Once the dispersive scales are destabilized, they typically spread all over the domain producing a very complicated spatio-temporal dynamics that is not captured by the NLCME.
- This behavior is the result of the competition of two effects: the dominating advection due to the group velocity and dispersion. It is interesting to notice that this is a generic situation that will be present in any propagative system with spatial reflection symmetry unless we manage to reduce the transport produced by the group velocity (e.g. by tuning the parameters to approach a

codimension two point).

- There are several recent rigorous proofs (see [6] and [36]) that establish that the solutions of the NLCME remain asymptotically close to solutions of the complete physical model (the MLE). This seems to be in contradiction with the results of this report, but this is not the case. These proofs do not contain any stability result and this is a stability issue: when a stable NLCME solution is dispersively unstable, its close MLE solution (without dispersive scales) is also unstable and the MLE dynamics likes to move away from this solution and develop dispersive scales, as the amplitude equations with small dispersive terms predict.
- The GS do not exhibit any dispersive instability. This result has been obtained from a linear stability analysis and has been checked against the numerical simulations of the amplitude equations with dispersion and the MLE. The reason for this behavior lies in the fact that this is a propagative instability and its growth requires the coupling that comes from the nonlinear interaction terms, but these terms go to zero as the perturbation travels away from the soliton center into its vanishing tails.

Summing up all the above remarks, we can conclude that, in general, the standard NLCME formulation fails to predict dynamics of the system and the material dispersion terms should be taken into account (i.e., eqs. (33)-(34) should be used) to appropriately describe the weakly nonlinear regime of light propagation in a fiber grating.

Appendix A. Numerical integration of the amplitude equations (33)-(35).

In this appendix we briefly describe the numerical method used to integrate the NLCME with dispersion terms (33)-(35).

The spatial periodicity of the problem (33)-(35) allow us to expanded its solution in finite Fourier series [37, 38] as

$$(A^+(x, t), A^-(x, t)) = \sum_{k=-\frac{N_F}{2}+1}^{\frac{N_F}{2}} (a_k^+(t), a_k^-(t)) e^{ik(2\pi x)},$$

using an appropriately large number of Fourier modes N_F . The resulting system of ordinary differential equations for the Fourier modes $(a_k^+(t), a_k^-(t))$ can be written as

$$\begin{aligned} \frac{da_k^+}{dt} &= c_k^+ a_k^+ + i\kappa a_k^- + n_k(a_j^+, a_j^-), \\ \frac{da_k^-}{dt} &= c_k^- a_k^- + i\kappa a_k^+ + n_k(a_j^-, a_j^+), \end{aligned}$$

where $c_k^\pm = \pm i(2\pi k) - i\varepsilon(2\pi k)^2$ and the nonlinear terms are given by

$$n_k(a_j^+, a_j^-) = [iA^+(\sigma|A^+|^2 + |A^-|^2)]_k.$$

In order to avoid numerical instability problems associated with the large values of the linear coefficients c_k^\pm for large k [39], we first rewrite the system of ODEs above in the form

$$\begin{aligned} \frac{d(e^{-c_k^+ t} a_k^+)}{dt} &= (i\kappa a_k^- + n_k(a_j^+, a_j^-)) e^{-c_k^+ t}, \\ \frac{d(e^{-c_k^- t} a_k^-)}{dt} &= (i\kappa a_k^+ + n_k(a_j^-, a_j^+)) e^{-c_k^- t}, \end{aligned}$$

where the linear diagonal terms are integrated exactly, and we then integrate it using a standard explicit fourth order Runge-Kutta method [39]. The resulting integration

scheme for a single time step of size Δt can be summarized as follows

$$a_k^\pm(t + \Delta t) = e^{c_k^\pm \Delta t} a_k^\pm(t) + \frac{\Delta t}{6} [e^{c_k^\pm \Delta t} K_{1k}^\pm + 2e^{c_k^\pm \Delta t/2} K_{2k}^\pm + 2e^{c_k^\pm \Delta t/2} K_{3k}^\pm + K_{4k}^\pm],$$

$$\begin{aligned} K_{1k}^\pm &= f_k^\pm(a_j^\pm(t)), \\ K_{2k}^\pm &= f_k^\pm(e^{c_j^\pm \Delta t/2} a_j^\pm(t) + \frac{\Delta t}{2} e^{c_j^\pm \Delta t/2} K_{1j}^\pm), \\ K_{3k}^\pm &= f_k^\pm(e^{c_j^\pm \Delta t/2} a_j^\pm(t) + \frac{\Delta t}{2} K_{2j}^\pm), \\ K_{4k}^\pm &= f_k^\pm(e^{c_j^\pm \Delta t} a_j^\pm(t) + \Delta t e^{c_j^\pm \Delta t/2} K_{3j}^\pm), \end{aligned}$$

where $f_k^\pm(a_j^\pm) = i\kappa a_k^\mp + n_k(a_j^\pm, a_j^\mp)$ and the only drawback of the scheme above is the fact that it requires to store the arrays of coefficients $e^{c_k^\pm \Delta t/2}$, which take into account the effect of the linear diagonal terms.

This integration procedure always handles the Fourier representation of the solution (a_k^+, a_k^-) . The solution is transformed to physical space only during the computation of the nonlinear terms, which is performed in the following steps

$$(a_k^+, a_k^-) \xrightarrow{\text{to Phys.}} (A^+, A^-) \rightarrow A^\pm(\sigma|A^\pm|^2 + |A^\mp|^2) \xrightarrow{\text{to Fou.}} n_k(a_j^\pm, a_j^\mp),$$

where the products of the amplitudes are computed in physical space and the so-called 2/3 rule is used to remove the aliasing terms (see e.g. [38]).

This numerical procedure has been implemented in a C code and the FFTW subroutines [40] have been used to perform the Fourier transforms. The typical resolutions used to integrate equations (33)-(35) with dispersion coefficient in the range $|\varepsilon| = .001, \dots, .001/16$ are $N_F = 256, \dots, 1024$ and $\Delta t = .01, \dots, .001$.

It is important to notice that the number of Fourier modes used for the numerical integration of eqs. (33)-(35) should not be too large since otherwise the long wavelength assumption (19) can be violated [31]. The correspondence between the wavenumber of the Fourier modes of the solution of the MLE and the wavenumber of the modes of the solution of the amplitude equations (33)-(35) is given by (see expression (13))

$$k_{\text{MLE}} = \pm 1 + \frac{2\pi}{L} k_{\text{AE}}, \quad \text{with} \quad \left(\frac{1}{L}\right) \sim |\varepsilon| \ll 1.$$

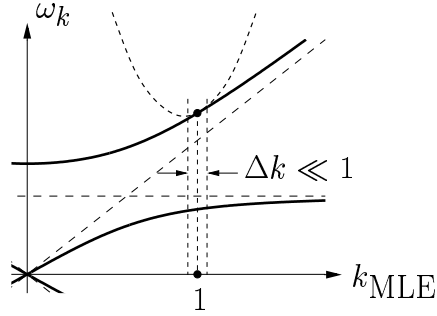


Figure 40: Dispersion relation of the original ML equations (solid line) and of the amplitude equations (33)-(35) (dashed line).

And the parabolic approximation produced by the amplitude equations to the true dispersion relation is only accurate for those modes of the MLE with wavenumbers near $k_{\text{MLE}} = \pm 1$ (see the dashed line in Fig. 31). In order to avoid spurious solutions of the amplitude equations with modes corresponding to wavenumbers away from $k_{\text{MLE}} = \pm 1$ (that are not damped because of the absence of dissipation in the system), and to ensure that the dispersive scales ($\sim \sqrt{|\varepsilon|}$) are properly represented in the numerical simulations, the following relation must hold between the dispersion coefficient $|\varepsilon| \ll 1$ and the number of Fourier modes used in the discretization of the amplitude equations:

$$\frac{1}{\sqrt{|\varepsilon|}} \ll N_{\text{F}} \ll \frac{1}{|\varepsilon|}.$$

The above problem does not arise in strongly dissipative systems in which the diffusive terms wipe out the high wavenumber modes.

Appendix B. Numerical integration of the MLE (16)-(17).

The Maxwell-Lorentz equations (16)-(17) with periodic boundary conditions in a spatial domain of size L ,

$$E(x + L, t) = E(x, t), \quad P(x + L, t) = P(x, t),$$

are integrated using in a numerical procedure completely similar to the one described in Appendix A, that is, using spatial discrete Fourier series expansions and a 4th order Runge-Kutta temporal scheme.

In order to do this, we first write the MLE as a first order system in terms of \dot{E} , E , \dot{P} and P ,

$$\begin{aligned} \frac{\partial \dot{E}}{\partial t} &= \frac{\partial^2 E}{\partial x^2} + \omega_p^2(1 - 2\Delta n \cos(2x))P - \omega_p^2(n_0^2 - 1)E - \omega_p^2 P^3, \\ \frac{\partial E}{\partial t} &= \dot{E}, \\ \frac{\partial \dot{P}}{\partial t} &= -\omega_p^2(1 - 2\Delta n \cos(2x))P + \omega_p^2(n_0^2 - 1)E + \omega_p^2 P^3, \\ \frac{\partial P}{\partial t} &= \dot{P}, \end{aligned}$$

and we then expand the solutions in discrete Fourier series,

$$(\dot{E}, E, \dot{P}, P) = \sum_k (\dot{e}_k(t), e_k(t), \dot{p}_k(t), p_k(t)) e^{i(2\pi k/L)x},$$

using an appropriately large number of Fourier modes. Note that it is enough to compute the modes with nonnegative wavenumbers because the electric and polarization fields are real fields and therefore verify

$$(\dot{e}_k, e_k, \dot{p}_k, p_k) = \overline{(\dot{e}_{-k}, e_{-k}, \dot{p}_{-k}, p_{-k})}.$$

The Fourier components of the grating term in the system above can be explicitly

computed to give

$$\begin{aligned} [2 \cos(2x)P]_k &= [(e^{i2x} + e^{-i2x}) \sum_j p_j e^{ij(\frac{2\pi}{L})x}]_k = \\ &= [\sum_j p_j (e^{i(j+n_L)(\frac{2\pi}{L})x} + e^{i(j-n_L)(\frac{2\pi}{L})x})]_k = p_{k-n_L} + p_{k+n_L}, \end{aligned}$$

where $n_L = L/\pi$, and the resulting system of ODEs for the Fourier modes of the solution can be finally written as

$$\begin{aligned} \frac{d\dot{e}_k}{dt} &= -(2\pi k/L)^2 e_k + \omega_p^2 (p_k - 2\Delta n (p_{k-n_L} + p_{k+n_L})) - \omega_p^2 (n_0^2 - 1) e_k - \omega_p^2 [P^3]_k, \\ \frac{de_k}{dt} &= \dot{e}_k, \\ \frac{d\dot{p}_k}{dt} &= -\omega_p^2 (p_k - 2\Delta n (p_{k-n_L} + p_{k+n_L})) + \omega_p^2 (n_0^2 - 1) e_k + \omega_p^2 [P^3]_k, \\ \frac{dp_k}{dt} &= \dot{p}_k, \\ \text{with } k &= 0, \dots, M. \end{aligned}$$

This system, with a sufficiently large number of modes M , is integrated using an explicit 4th order Runge-Kutta method. The computation of the nonlinear term is carried out in physical space as explained in Appendix A and the discrete real Fourier transforms are performed using the FFTW routines [40].

References

- [1] C. Martijn de Sterke and J.E. Sipe, “Gap Solitons”, in Progress in Optics XXXII, E. Wolf ed., 1994.
- [2] A. B. Aceves, ”Optical gap solitons: past, present and future; theory and experiments”, CHAOS **10** (2000) 584-589.
- [3] G. Kurizki, A. E. Kozhekin, T. Opatrny and B. Malomed, “Optical solitons in periodic media with resonant and off-resonant nonlinearities”, in Progress in Optics 42, E. Wolf ed., 2001.
- [4] G. P. Agrawal, Nonlinear Fiber Optics, Optics and Photonics series, Academic Press, San Diego, 1995.
- [5] W. Lauterborn, T. Kurtz and M. Weisenfeldt, “Coherent Optics: Fundamentals and Applications”, Springer Verlag, Berlin, 1993.
- [6] R.H. Goodman, M.I. Weinstein and P.J. Holmes, “Nonlinear propagation of light in one-dimensional periodic structures”, J. Nonlinear Sci. **11** (2001) 123-168.
- [7] M.P. Sørensen, M. Brio, G. M. Webb and J.V. Moloney, “Solitary waves, steepening and initial collapse in the Maxwell-Lorentz system”, Physica D **170** (2002) 287-303.
- [8] A. Hasegawa, “Optical Solitons in Fibers”, 2nd edition, Springer-Verlag, Berlin, 1990.
- [9] M.C. Cross and P.C. Hohenberg, “Pattern formation outside equilibrium”, Rev. Modern Phys. **65** (1993)851-1112.
- [10] A.B. Aceves and S. Wabnitz, “Self-induced transparency solitons in nonlinear refractive periodic index”, Phys. Lett. A **141** (1989) 37-42.
- [11] D.N. Christodoulides and R.I. Joseph, ”Slow Bragg solitons in nonlinear periodic structures”, Phys. Rev. Lett. **62** (1989) 1746-1749.
- [12] A. de Rossi, C. Conti and S. Trillo, “Stability, multistability and wobbling of optical gap solitons”, Phys. Rev. Lett **81** (1998) 85-88.

- [13] I.V. Barashenkov, D.E. Pelinovsky and E.V. Zemlyanaya, “Vibration and oscillatory instabilities of gap solitons”, *Phys. Rev. Lett.* **80** (1998) 5117-5120.
- [14] I.V. Barashenkov and E.V. Zemlyanaya, “Oscillatory instabilities of gap solitons: a numerical study”, *Comp. Phys. Comm.* **126** (2000) 22-27.
- [15] C. M. de Sterke, “Simulations of gap-solitons generation”, *Phys. Rev. A* **45** (1992) 2012-2018.
- [16] R.E. Slusher, B.J. Eggleton, T.A. Strasser and C.M. de Sterke, “Nonlinear pulse reflection from chirped fiber gratings”, *Optics Express* **3** (1998) 465-475.
- [17] C.M. de Sterke, “ Theory of modulational instability in fiber Bragg gratings”, *J. Opt. Soc. Am. B* **15** (1998) 2660-2667.
- [18] B.J. Eggleton, C.M. de Sterke and R.E. Slusher, “Bragg solitons in the nonlinear Schrödinger limit: experiment and theory”, *J. Opt. Soc. Am. B* **16** (1999) 587-599.
- [19] N.M. Litchinister, B.J. Eggleton, C.M. de Sterke, A.B. Aceves and G.P. Agrawal, “Interaction of Bragg solitons in fiber gratings”, *J. Opt. Soc. Am. B* **16** (1999) 18-23.
- [20] N.M. Litchinister, C.J. McKinstrie, C.M. de Sterke and G.P. Agrawal, “Spatiotemporal instabilities in nonlinear bulk media with Bragg gratings”, *J. Opt. Soc. Am. B* **18** (2001) 45-54.
- [21] K. Ogusu, “Effect of stimulated Brillouin scattering on nonlinear pulse propagation in fiber Bragg gratings”, *J. Opt. Soc. Am. B* **17** (2000) 769-774.
- [22] D. Pelinovsky, J. Sears, L. Brzozowski and E.H. Sargent, “Stable all-optical limiting nonlinear periodic structures. I. Analysis”, *J. Opt. Soc. Am. B* **19** (2002) 43-53.
- [23] D. Pelinovsky and E.H. Sargent, “Stable all-optical limiting nonlinear periodic structures. II. Computations”, *J. Opt. Soc. Am. B* **19** (2002) 1-17.
- [24] O. Zobay, S. Pötting, P. Meystre and E.M. Wright, “Creation of gap solitons in Bose-Einstein condensates”, *Phys. Rev. A* **59** (1999) 643-648.
- [25] P.G. Daniels “Finite amplitude two-dimensional convection in a rotating system”, *Proc. R. Soc. Lond. A* **363** (1978) 195-215.
- [26] C. Martel and J.M. Vega, “Finite size effects near the onset of the oscillatory instability”, *Nonlinearity* **9** (1996) 1129-1171.
- [27] C. Martel and J.M.Vega, “Dynamics of a hyperbolic system that applies at the onset of the oscillatory instability”, *Nonlinearity* **11** (1998) 105-142.
- [28] A.R. Champneys, B.A. Malomed and M.J. Friedman, “Thirring soliton in the presence of dispersion”, *Phys. Rev. Lett.* **80** (1998) 4169-4172.

- [29] A.R. Champneys and B.A. Malomed, “Moving embedded solitons”, *J. Phys. A: Mat. Gen.* **32** (1999) L547-L553.
- [30] J. Schöllmann and A.P. Mayer, “Stability analysis for extended models of gap solitary waves”, *Phys. Rev. E* **61** (2000) 5830-5838.
- [31] C. Martel, J.M. Vega and E. Knobloch, “Dynamics of counter-propagating waves in parametrically driven systems: dispersion vs. advection”, *Physica D* **174** (2003) 198-217.
- [32] T. Kapitula, “The Evans function and generalized Melnikov integrals”, *SIAM J. Math. Anal.* **30** (1998) 273-297.
- [33] Y.A. Li and K. Promislow, “The mechanism of the polarizational mode instability in birefringent fiber optics”, *SIAM J. Math. Anal.* **31** (2000) 1352-1373.
- [34] B. Sandstede, “Stability of travelling waves”, in *Handbook of Dynamical Systems II*, B. Fiedler ed., Elsevier, 2002, 983-1055.
- [35] L.W. Ahlfors, “Complex Analysis”, McGraw-Hill, 1966.
- [36] G. Schneider and H. Uecker, “Nonlinear coupled mode dynamics in hyperbolic and parabolic periodically structured spatially extended systems”, *Asymptotic Analysis* **28** (2001) 163-180.
- [37] D. Gottlieb and S.A. Orszag, *Numerical Analysis of Spectral Methods: Theory and Applications*, SIAM-CMBS vol. 26, 1977.
- [38] C. Canuto, H.Y. Hussani, A. Quarteroni and T.A. Zang, *Spectral Methods in Fluid Dynamics*, Springer Series in Computational Physics, Springer-Verlag, 1988.
- [39] J.D. Lambert, *Numerical Methods for Ordinary Differential Systems: The Initial Value Problem*, John Wiley and Sons, 1995.
- [40] M. Frigo and S.G. Johnson, *FFTW User’s Manual*, 1999 (available at <http://www.fftw.org>).